THESIS FOR THE DEGREE OF DOCTOR OF PHILOSOPHY (PhD)

Perspectives of Imaging Cytometry and its implication on High content screening

by Minh Doan, MD

Supervisor: Dr. Zsolt Bacsó, MD, PhD

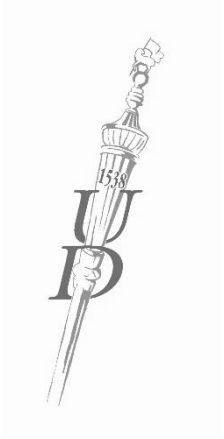

UNIVERSITY OF DEBRECEN

DOCTORAL SCHOOL OF MOLECULAR CELL AND IMMUNE BIOLOGY

DEBRECEN, 2015

Table of contents

List of Abbreviations

AD	atopic dermatitis
AV	Annexin V
CAD	caspase-activated DNase
CCD	charge-coupled device
CFP	cyan fluorescent protein
DC	dendritic cells
FRET	fluorescence resonance energy transfer
FSC	forward side scatter
HCS	High-content screening
HTS	High-throughput screening
LSC	laser scanning cytometry
mDC	myeloid dendritic cells
Pb	photobleaching
PBMC	peripheral blood mononuclear cell
PMEF	primary mouse embryonic fibroblast
PMT	photomultiplier tube
QC	quality control
ROI	region of interest
SEB	Staphylococcal enterotoxin B
SGBS	Simpson- Golabi- Behmel syndrome
SSC	side scatter
Th	T-helper cell
TNFα	tumor necrosis factor alpha
TSLP	thymic stromal lymphopoietin
YFP	yellow fluorescent protein

1. Introduction

1.1 An overview of cytometry techniques

Knowledge regarding the complexity of a cell has grown tremendously over the last century. The infinite changes that can occur in an individual cell under different conditions represent a myriad of data for scientists to mine. Through the marvels of 21st century technology, cell biologists have witnessed major technological advances that have led to a steady development of cellular measurements.

In the late 1940s, Wallace Henry Coulter introduced the cell counter. This was the first flow cytometric system, in which the impedance was used for counting and sizing suspended cells in conducting liquids. Later in the 60s and 70s, fluorescence-based flow cytometry was developed and became a dominating method for objective cell measurement (1). The key concept in cytometry is to collect and evaluate physical and chemical characteristics of single cells, and at the same time taking into account statistical distribution of these parameters in cell populations. This concept defines the fundamental concern of cytometric measurements: to collect whole cell signals of the questioned parameters. Although flow cytometry could satisfy this requirement and is indeed a powerful multiparametric tool to reveal heterogeneity of cell populations, sampled cells should be in suspension, meaning that cultured adherent cells should be detached mechanically or enzymatically. These treatments can interfere with cellular parameters to be investigated. Due to the nature of operation, original flow cytometry system gives only one value in a channel for one flow-by cell; if there is a cellular change upon stimulus, flow cytometry cannot provide information about the time course of a response in a single cell. Newer automation of flow cytometry involved the construction of sample chambers to allow on-line addition of reagents (2,3) and later more automation has been adapted into flow cytometry for acquisition of time-dependent data (4). However, these solutions still could not provide the ability to revisit and track changes in a specific cell, as million cells flows by detectors in each measurement. In addition, due to the lack of photographing ability, the intracellular pattern of a cell can hardly be studied. Until recently, new development of streaming flow cytometry has emerged, featuring imaging capacity to a flow cytometry system to solve the limitation in term of pattern analysis (5,6).

Image cytometry is a rapidly developing modality of cytometry and is in fact the oldest form of cytometry, which traditionally presented in the form of using microscopy to subjectively observe and describe cells, stemming from the work of Leeuwenhoek in 1673 (7). Image cytometers operate by micro-photographing a large number of cells, getting whole cell information from image analysis and generating statistics of cell properties. Prior to measurement, cells are commonly labeled or stained by fluorochromes or chromatics to enhance contrast or to detect specific molecules (8). This technique yields visual information at the single-cell level, a type of information that is not available through other approaches. Resolution of sub-cellular structures, and analysis of cells in situ, can be achieved only by microscopy. Similarly, time-course measurements in single cells can be also obtained (9). Image acquisition was traditionally done manually by microscope users. Thus low statistical accuracy is one of the disadvantages of conventional microscopic measurements, since only a relatively small number of cells can be investigated within a reasonable time frame. These labor-intensive and time-consuming systems are often incompatible with high-throughput strategies.

Since the introduction of the digital camera and computational image analysis, in the mid-1990s, the automation level of image cytometers has steadily increased. This has led to the commercial availability of automated image cytometers, ranging from simple cell counters to sophisticated screening systems (10). Quantitative imaging cytometry is although recently introduced in the past two decades, it soon became the technology of choice for high-content (HCS), high-throughput (HTS) screening of cellular and tissue samples.

1.2 Current advancements of image cytometry

At the dawn of screening technology, two aspects that determined directions of the technological developments were the focus and exposure, which are two major factors that affected deeply the quality of an automated screening campaign (11).

An out-of-focus image, even slightly, will impact the apparent size and intensity of the objects and sub-objects within the image, and can quickly increase the noise within the analysis (11,12). Primary technology expansions in laser scanning imaging improved the auto-focus capabilities of the systems. Now, most platforms provide multiple ways to auto-focus fields with acceptable robustness and speed.

Previously, scanning systems were often built with spherical lenses, those that can only image along a circular surface. Off axis deflection through a focusing spherical lens system will generally form aberrated images in a curved surface as opposed to a more desirable flat plane (13). In recent developments, a flat field scanning lens is thus engineered, in which the focal plane of a deflected laser beam is a flat surface. In more innovative laser machinery, F-theta lens is such an example of flat scanning lens. F-theta scan lenses are used in conjunction with XY galvanometer scanner to form a correct and large enough two dimensional scanning area. The scan lens is optimized to provide a flat field image with diffraction-limited spot size in micron scale over the entire scan field. This approach makes possible to digitalize the whole surface of a well of the sample plate using only one location of the objective, since the focus distance (F) is directly proportional to the scan angle (theta). Typically, with the F-theta linearity image distortion is kept less than 1% without the need for further software corrections to minimalize image distortion (13).

In order to register a satisfactory brightness on a detector, the sample is illuminated for a certain duration, also known as the exposure time. Long exposures complicate photography of specimens by increasing the likelihood of undesirable photobleaching, phototoxicity, and blurring by vibration. High speed instruments tend to use shorter exposure times to increase high throughput, but this may sacrifice resolution. Thus, a good exposure is crucial and is often taken care of by two widely used technological directions in scanning microscopy: wide-field illumination coupled with charge-coupled device (CCD) cameras or laser beam illumination coupled with photo multiplier tubes (PMT).

Wide-field illumination is a method of both supplying excitation light to, and collecting emitting light from, a large area of a sample. This allows users to survey a wide area with low-magnification objectives, maximizing the number of cells per image, and photobleaching can be reduced by short exposure times. This practice would require a high performance CCD camera that is sensitive to low-light signals on a large area of parallel-processed “megapixels”.

Laser beam illumination coupled with PMT is another principle to develop clear signals in cytometers. Photomultipliers contain a photosensitive surface that captures incident photons and produces a stream of photoelectrons to generate an amplified electric charge. As a result, signals from single-pixel-small area, even with a short illumination by a laser beam, can still be captured, enhanced by PMTs and be detected. In term of irradiance, which is the illuminating

radiation power per unit area, in watts per square meter (W/m^2), laser beam illumination is of million times stronger compared to wide-field illumination (14). One pixel detection sensitivity by a PMT is of thousand times larger compared to the sensitivity of one pixel on a CCD chip (15). Furthermore, the PMT has a larger dynamic range, better linearity, but less quantum efficiency. Altogether, PMT is thus more sensitive on one pixel and unit time basis. In an imaging system, the region of interest (ROI) is sampled by raster scanning of a laser beam (with the help of oscillating mirrors, see Instrumental settings). This type of scanning mode indeed provides more concentrated illumination for pixel-small areas and thus yields better illumination with shorter exposure time.

When comparing speed of performance, wide-field illumination coupled with CCD camera is considered being faster since it captures one field image megapixel-wise, as opposed to beam illumination coupled with PMTs, in which single pixels is processed at a time. For screening purposes that pursuit high throughput while moderately demand on high content, wide-field imaging by CCDs are more favorable. For example, when screening cell health, one would shorten the measuring time not to keep cells out of the culturing incubator for too long, while the signals of vital staining by Annexin V and propidium iodide do not require high resolution. However, in CCDs, the image pixels are recorded on the chip and then one by one sent through the analog to digital converter to build the data. Due to this principle, there is a practical limit to the size of CCDs because of the time required to read them out. Therefore, the physical size of CCDs cannot increase to infinity; in fact, they are typically small, and it consequently can image only a small region at a time. In order to image a larger area, the large area has to be divided into smaller regions that fit to the size of a CCD sensor. Each of such small regions is then imaged and in the end combined together in an act known as stitching images. This necessity of stitching images together is computationally time consuming and making impossible to apply in real time measurements.

Of note, in slide-based cytometry, where cellular objects are placed on plastic or glass surface, this signal enhancement may adversely increase noise from background since every pixel across the surface of scanning area will be amplified. But this is not the case in flow cytometry, where background practically does not exist, thanks to the suspension of the object in fluidic droplets. Thus, in term of dynamic range and speed of acquisition, slide-based cytometry is considerably less sensitive and slower than that of flow cytometers, respectively.

Many artifacts can confound image analysis, including out-of-focus signals, debris, overexposure, and fluorophore saturation, among others. Because these anomalies vastly affect valuable measurements, quality control (QC) is critical in high-throughput and high-content screening. Conventionally, QC can be evaluated by the comparison of signal-to-noise ratio (S/N) and signal-to-background ratio (S/B). However, S/B does not take into account any information on variability of the signals; and S/N can capture the variability only in one group and hence cannot assess the quality of assay when the two groups, treated and not treated ones, have different variability (16). Zhang J.H. et al. (17) proposed Z-factor, with the advantage over S/N and S/B is that it takes into account the variability in both compared groups. The Z-factor is defined in terms of mean (μ) and standard deviation (σ) of positive (+) and negative (-) samples, and calculated as $Z = 1-(3[\sigma(+)+\sigma(-)]/[\mu(+)-\mu(-)])$. This metric quantifies the separation between the experimental and control treatments, while remaining sensitive to intra-treatment variation. Data that yielded $0.1 < Z < 0.5$ reflects "good" assay suitability for HTS, while $0.5 < Z < 1$ reflects "excellent" assay suitability (17).

In another approach for QC, Zhang X.H.D. (16) proposed the strictly standardized mean difference (SSMD) as a measure of effect size, and a measure of the differentiation between groups. SSMD is the mean divided by the standard deviation of a difference between random values each from one different group. SSMD has a strong link with the probability that the difference between two groups is positive (d+-probability) (18). SSMD allows the differentiation between large and small effects of treatments and maintains flexible and controlled selection for both false-negative and restricted false-positive events, represented by direct assessment of the difference between treated and negative controls; whereas it is nontrivial for the classic z-score method and t-test to control the false negative rate. SSMD can generally be applicable to any assay, in which the expectation is a difference in signals between treated and non-treated reference sample.

1.3 Slide-based imaging cytometric applications

The *laser-scanning cytometer* (LSC) is a representative instrument of high-content quantitative technology and is a microscope-based cytofluorometer, which has attributes of both flow cytometry and microscopy. Although having a flow cytometry heritage, it is not limited to analyzing cells in mobile fluids (19,20). In contrast, it allows automated analysis of stationary samples, including adherent cultured cells and tissues attached to microscopic slides

with minimized perturbation, preserving the sample structure and vitality (21,22). Its versatility opens up a wide range of applications, enables many cellular and tissue-based analysis throughout the biomedical sciences and pharmaceutical discovery. Fields of application may include but not limited to cell cycle analysis, immunophenotyping, quantitative histology, cell health analysis, and pharmacology/toxicology.

Cell cycle analysis is a classic example of cytometric measurements in general and of LSC in particular. A large number of DNA fluorochromes can be used for DNA content analysis and a great variety of techniques has been published during the past three decades. In his review, Darzynkiewicz (23) has shown general principles of instrumentation and cell analysis to assess DNA ploidy. One may directly measure of the total fluorescence of a nuclear dye (e.g. DAPI, Hoechst, Propidium Iodide etc.), which is proportional to the DNA content. The DNA content histogram explicitly shows cell populations in sub-G1, G1, G2 and S phases. Such robust cell phase profiling was very well appreciated when screening xenobiotic effects in 96-well or 384-well plates.

When only a small number of cells are available—often the case with fine-needle aspirates or tissue samples—immunophenotyping is not possible applying traditional flow cytometry. For instance, Al-Za'abi et al. (24) have proven the equivalence of laser scanning cytometric and flow cytometric immunophenotyping of lymphoid lesions in cytological samples. Moreover, LSC offers significant advantages: cell immunophenotype can be linked to cell morphology, and cells can be reprocessed in situ with cytoplasmic, immunological, or genetic markers. Tarnok et al. (25) has emphasized that LSC is a convincing technology particularly in immunophenotyping of neonates at various sampling times without substantial blood loss (e.g., for rational decision making in neonatal sepsis or for risk assessment in pediatric cardiac surgery). Smaller sample volume needed is of special importance when only small sample volumes are available such as biomaterials taken from small children.

Clinical diagnoses of different diseases, especially in oncology, require examinations of tissue and cell pathology. Previously, this task was heavily dependent on a trained cellular pathologist. Recently, when LSC was used in routine histopathology and immunohistochemistry, its automated quantitative capability offered outstanding efficient data collection without inter-observer variation. Peterson et al. (26) have demonstrated that LSC is capable of detecting cells on histo-cytological samples by using either autofluorescence,

chromatic staining or fluorescent signals for automated segmentation of cells. It thus allowed high content and reliable quantification in such clinical application with objective manner.

LSC also exhibits its strength in investigation of cell proliferation, cell health and cell death. Thanks to its slide-based concept, adherent cultured cells and tissues attached to microscopic slides can be measured directly, during which the physiological conditions surrounding the cells can be even kept. In a plausible publication, Nombela-Arrieta et al. (27) displayed the development of hematopoietic stem and progenitor cells in the bone marrow microenvironment. In this work, living stem cells and their cell-specific mechanisms against minimally oxygenated niche were delicately monitored with the aid of LSC.

In another example, by combining vital and non-vital assays, Bacso et al. (21) showed that the DNA of Annexin V-positive (AV+) cells was highly fragmented. AV fluorescence (after vital staining) and SYBR-Gold fluorescence of DNA (after cell lysis in halo assay) of the same Jurkat cells were measured following treatment with anti-Fas. The data from both sets of measurements were merged (overlaying images of pre- and post-treatments), allowing direct correlation of membrane and nuclear markers of cell death. This technique allowed accurate distinction between apoptotic and necrotic cells and cytometric grading of apoptosis.

Darzynkiewicz et al. (28,29) have also addressed the analysis of apoptotic cells and DNA strand breaks using LSC, and illustrated how visual examination of the presumed apoptotic cells detected by cytometry makes it possible to clarify the engulfment process of monocytes/macrophages, in which they ingested nuclear fragments via apoptotic bodies. From these works, the characteristics of plasma membrane, intracellular organelles (e.g. mitochondria, nucleus etc.) and subcellular structures (e.g. chromatins, apoptotic bodies) of the cells undergoing different processes were well illustrated under the scope of LSC.

Cytometric techniques have been regularly applauded in pharmacology/toxicology, especially in drug discovery, as shown by the work of Swinney et al. (30). Pharmaceutics thrive from both molecular and empirical approaches. The molecular strategies are predominantly hypothesis-driven and are referred to as target-based. The empirical approaches are referred to as phenotypic screening. A recent analysis by Swinney has revealed the latter to be the more successful strategy.

2. Aims of study

In the era of the emerging artificial intelligence, there is a growing desire to build unbiased cytometric platforms that can harvest multiple parameters from single cells in a high throughput manner independently of the subjective human. Such platforms are exquisitely appropriate to use in histo-cyto-pathology screening, where discrepancies among human examiners should be minimized, and giving rise to a reliable diagnosis. In another significant instance, the high-content *and* high-throughput of such a platform are the essences of empirical phenotype-based screening in drug discovery.

In light of these contemporary trends, our ultimate goal is to develop and establish multiplex protocols, for either flow or imaging cytometry, which can be utilized for a broad variety of purposes. Once established, such a platform would provide scientists a ready protocol to utilize across many research and health care fields.

This dissertation aims to exemplify the adoption of LSC to characterize biological systems as demonstrated in the studies of **1**-adipocyte differentiation, **2**- DNA damage detection, **3**- protein interactions, and **4**- signaling pathways in dendritic cells.

2.1 High-content analysis of adipocyte differentiation

Researchers have tackled the issue of obesity with great attention since it is a major risk factor for a number of chronic diseases, including diabetes, cardiovascular diseases, and cancer (31,32). As adipocyte biology is involved in those significant medical conditions, adipogenesis- where adipocytes develop from mesenchymal stem cells- has been extensively studied in recent years (32,33).

In current studies, multiparametric model systems are being developed, where adipocyte differentiation, its nuclear, cytoskeletal and sub-organellar morphological changes can be monitored together with different drug applications in an automated manner. Noticeably among these works, Lee had introduced a flow cytometric assay to assess differentiation of preadipocytes, based on cytoplasmic granularity changes corresponding to lipid droplet accumulation (34). Application of flow cytometry, however, requires cell suspensions, which strongly violates physiological optima of solid tissues and this technique omits the possibility of *in situ* visualization and reanalysis of samples attached to a culture dish. These latter

obstacles were solved by applying image cytometry in solid tissue quantifications, as in Lin's work, where laser scanning cytometry was utilized to study adipocytes and measure capacity of drugs to induce adipocyte apoptosis (35,36). In their study, cell recognition of attached cells was not solved or at least not clearly explained whether single cell contouring or phantom contouring was used. When attached cells get more confluent during their culturing, cell-by-cell segmentation becomes challenging and requires sophisticated algorithms and tools. There have been a few attempts to enable cell-by-cell analyses (37-39), e.g. McDonough et al. (37,38) introduced an algorithm to recognize cells in confluent cultures and a later study applies this algorithm (39). Yet, their assumptions that preadipocytes or adipocytes cover all the surface of a culture disk and, more importantly, that nuclei are located in the center of cells, seems inapplicable for human fat cells. Currently, there is no satisfactory quantitative study about human adipogenesis that focuses on single-cell imaging cytometry, and none of them would be efficiently adaptable for high throughput applications.

Here we would like to introduce a cytometry approach that could inspect adipocytes at different time points throughout their differentiation, quantitate single cells in a high-content manner yet in physiologically conservative conditions and could conveniently study both adipocytes and preadipocytes simultaneously in a slide-based platform.

2.2 LSC application for DNA damage detection

Cellular DNA content and integrity have been the objects of interest from the dawn of cell biology. With the help of fluorochromes, the chromatin and nuclear infrastructure can be readily inspected using high resolution microscopy. LSC has been found exceptionally useful in screening for DNA damage, especially during apoptosis, thanks to its ability to analyze cellular DNA on microscopic slides (21,40-42). Only with such slide-based technique could the cell-by-cell DNA evaluation of disrupted cells be performed with high accuracy, in contrast to flow cytometry, where necrotic debris and apoptotic bodies would disassociate away from sampled cells.

Various studies have been done to demonstrate the capability of LSC in quantification of DNA damage (21,29). Here we focus on the investigation of DNA damage that occurs during normal cell differentiation. This interest arose from the signs of nuclear condensation previously seen during the differentiation process of adipocyte (43).

2.3 High throughput analysis of protein-protein interactions

The precise location and nature of the interactions between specific molecular species in living cells is of major interest in many areas of biological research (44,45). Examining these phenomena is however often hampered by the limited resolution of the instruments employed. Conventional wide-field fluorescence microscopy enables only the localization of fluorescent-labeled molecules within the optical spatial resolution limits, approximately 200 nanometers, called Abbe-limit. However, in order to understand the physical interactions between protein partners involved in a biochemical process, the relative proximity of the molecules must be determined precisely and it should not be limited by the diffraction, as it is in the conventional imaging methods. The technique of fluorescence resonance energy transfer (FRET), when applied to optical microscopy, permits the investigation of distances within several nanometers, which is sufficient for monitoring particular molecular interactions. Leuchowius et al. (46) demonstrated the power of their assay of in situ proximity ligation analysis for the determination of heteroassociation of members of the EGF family by flow cytometry. Here, we demonstrate that by using ECFP and EYFP protein as FRET reporters, the interaction of Fos and Jun proteins in living adherent HeLa cells can be elucidated. We define the methodology for semi-automated FRET measurements uniting the high throughput with the capability of subcellular resolution and cell backtracking in a single instrument. Our method can facilitate screening of protein interactions by using FRET-based LSC assays.

2.4 Elucidation of signaling pathways in a limited amount of dendritic cells

In clinical research, the limited size of obtainable sample is usually a difficult issue, this is particularly true when collecting hematological samples from pediatric patients or patients in critical conditions. As an example, atopic dermatitis (AD) is an inflammatory, chronically relapsing and pruritic skin disorder, which affects millions of children every year. In AD, myeloid dendritic cells (mDCs) are actively involved in the initiation and maintenance of skin inflammation, and the enhanced migration of these cells coincides with the eruption of skin lesions. The tissue microenvironment tightly controls mDC activation, which initiates the differentiation and lineage commitment of several skin-infiltrating T helper (Th) subpopulations.

However many studies have failed to characterize the role of dendritic cells in this condition, because mDCs collected directly from patients are usually present in an amount that is too low for a flow cytometric approach to perform a full landscape of phenotyping. By using laser scanning cytometry, we intend to show here the examination of the cytokine expression profile de novo and the modulation of the T cell-polarizing cytokine production of myeloid DCs from AD patients.

3. Materials and Methods

3.1 Instrumental settings

The utilized LSC instrument was iCys research imaging cytometer (CompuCyte Corporation, Westwood, MA), a computer-controlled 0.5-micron spot size laser scanning cytometer. It was based on an inverted microscopic platform equipped with three lasers (488 nm argon-ion laser, 633 nm HeNe laser, and 405 nm solid-state lasers), photodiodes (detecting light loss and scatter) and four photomultiplier tubes (PMTs). A series of dichroic mirrors were built to direct laser beams (Figure 1). A second-stage dichroic mirror reflected the laser light toward the sample and it also transmitted fluorescent lights emitted from sample to the direction of the photomultiplier tube (PMT) detectors. Each laser beam was shuttered under computer control. A single beam or several combined beams were steered to a computer-controlled scanning mirror that oscillates to create a scan line at the specimen. After passing through a scan lens, the beam entered the side port of an Olympus IX71 inverted microscope and focused onto the focal plane of the specimen (22).

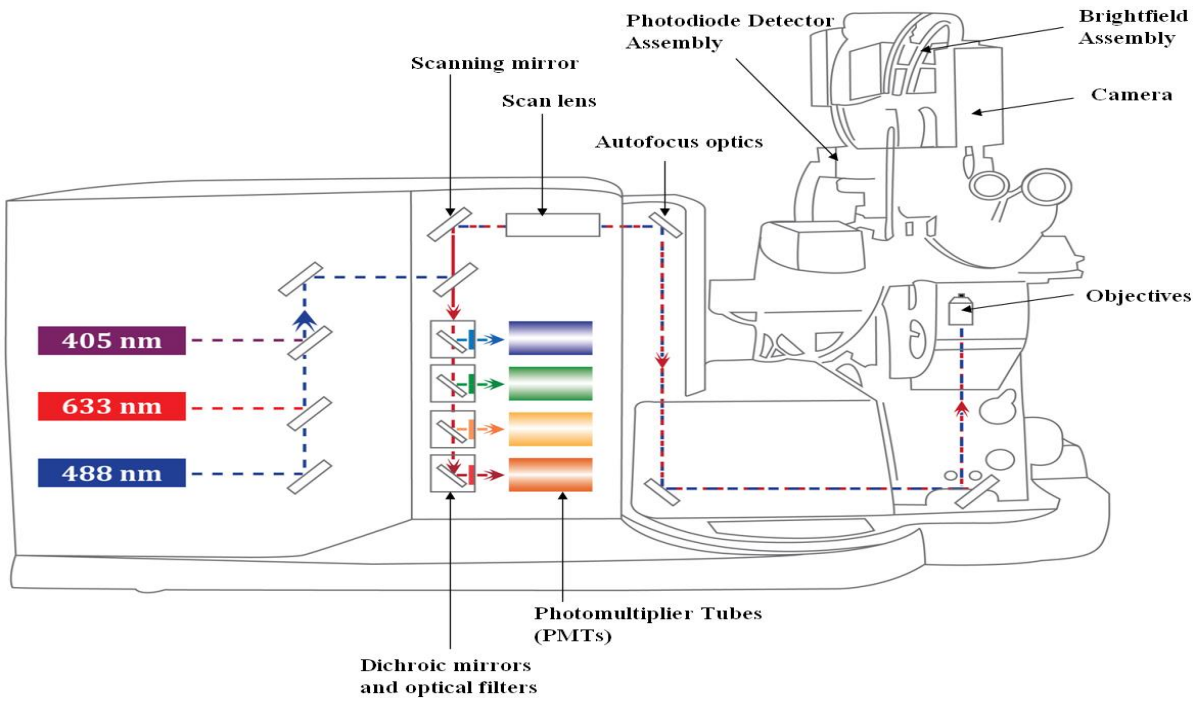

Figure 1. iCys Optical System

The specimen carrier was mounted in a holder on a computer-controlled, motor-driven stepper stage. The stage moved in adjustable steps. Picture elements were built into scan field

images from this raster scan motion. The fluorescent light emitted at each pixel location was collected by the objective lens and steered through the scan lens to the scanning mirror. At first, this emitted fluorescent light was collimated, then it passes through a series of filter cubes containing dichroic mirrors and optical interference filters to the photomultipliers (defining the emission channels accordingly), each detecting a specific fluorescence wavelength range.

User-defined areas on the specimen having optimal cell density were marked as regions of interest (ROIs) and scanned in an automated process. Each ROI was divided into smaller areas called scan fields by the software. Each scan field (1024×768 pixels) was scanned by a focused laser beam via an oscillating mirror in the y direction and by the motorized stage in the x direction with a step size adjustable from 0.05 to 20 μm. The arising fluorescence signals were collected via objectives, whereas transmitted light was captured by the light loss detector photodiodes. Size of a pixel can be set according to the purpose of the measurement, typically for general cellular measurement at 0.25 by 0.245 micrometer using 40× magnification objective, NA 0.75.

3.2 Analytic algorithms and softwares

The companion analyzing software iCys 7.0 (iNovator Application Development Toolkit, CompuCyte Corporation, Westwood, MA, USA) (Figure 2) and CellProfiler (Broad Institute of MIT, MA) (47), (48) (Figure 3) were used. Physical analog signals were converted to digital imaging data. By using one or a combination of these signals, cellular objects or cellular organelles were automatically recognized by a process called segmentation of the image, i.e. discrimination of cells from background. Membrane staining signals were used to define an event as a cell, and marked by contours (Figure 4), the boundaries within which pixels were higher than certain threshold values (Figure 4 top left, "profile view").

Fluorescent intensity, forward light scattering, area, perimeter, circularity, location, and other profiles of the cellular events were assembled individually by the software. The integral fluorescent intensity (Integral) and maximal pixel intensity (MaxPixel) were defined as sum of the pixel intensities and the peak value within a cellular event, respectively. The division of integral signal by total area of an event in agreement to the pixel size gave rise to the mean pixel intensity (Intensity). Data of cellular events as *bit* pattern images also underwent arithmetic calculations, such as addition, subtraction, or inversion in some specific need. The

collected data from the cytometer was eventually exported to spreadsheet programs, namely FCS Express, GraphPad Prism, and Microsoft Excel, for further data evaluation and calculation.

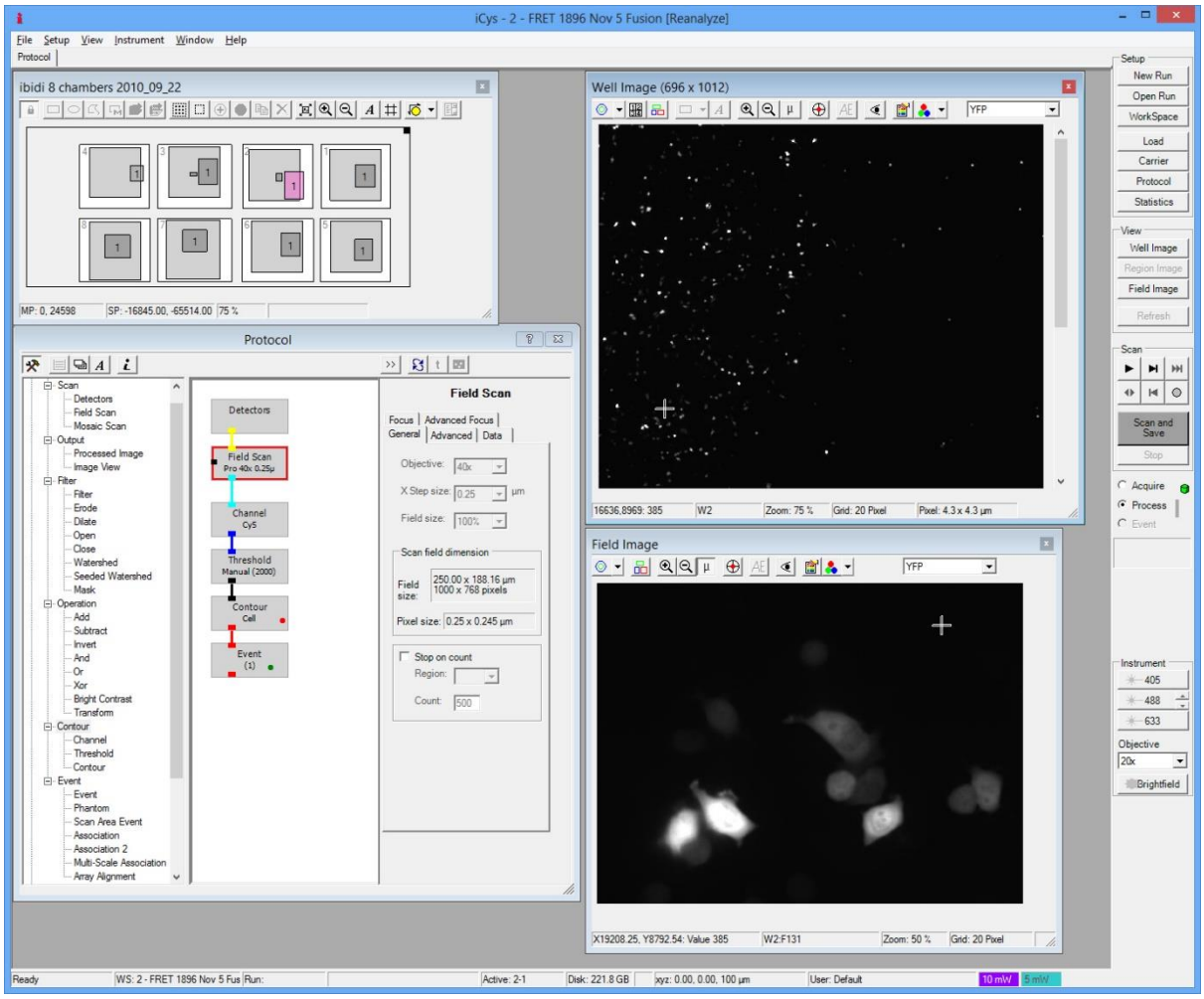

Figure 2. Typical interface of iCys 7.0 Cytometric Analysis Software. The interface categorizes modules into interactive windows. Top left: "Carrier" window with a sketch of an 8-well ibidi chamber, where the user defined Regions of interest (ROIs). Top right is the "Well image" landscape generated by a scout scan of the ROI (pink area in "Carrier" window). White dots in the black background are Cy5 labeled cells. Lower right is a detailed "Field image" at the cross hair of the top right "Well image", where the user can visualize cellular objects with higher resolution. The two cross hairs of the top- and lower right windows point at the same spot in the 8-well chamber. Lower left: "Protocol" window is where the user can construct a pipeline to adjust system settings and design a measurement, e.g. selecting lasers, adjusting the laser power, and selecting channels.

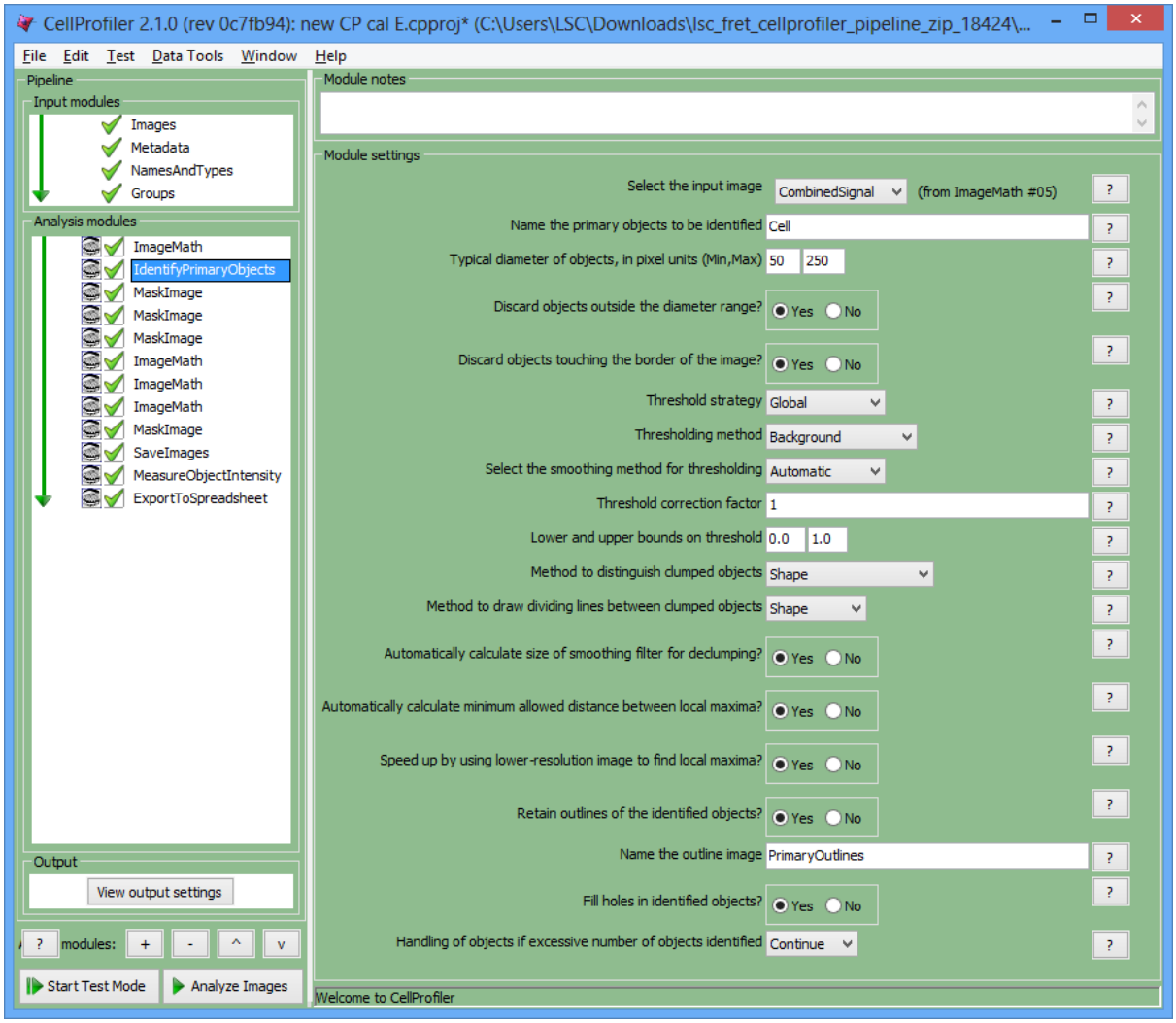

Figure 3. Typical interface of image processing pipeline in CellProfiler to analyze data. A CellProfiler pipeline consists of algorithmic steps. Left panel (white area): series of modules, each module performing a specific processing task. The arrow indicates the direction of data processing, i.e. the outputs of upstream steps are the inputs for subsequent steps. Three main sections of a pipeline are: Input modules (upper-left), where the user compiles a list of files to be analyzed, assigns names and metadata to images and constructs groups; Analysis modules (middle-left), where the user builds analytical steps to process images and extracts values from measurements; Output (lower-left): the settings for default input and output locations. Right panel (green area): detailed parameters and settings for each module.

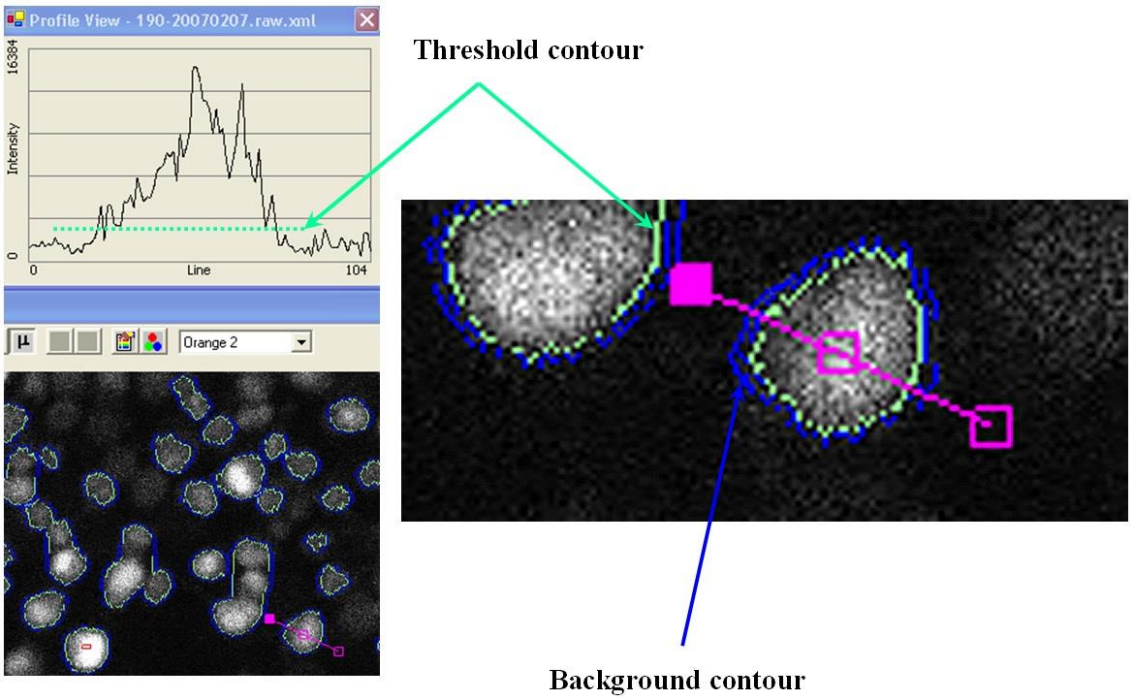

Figure 4. Contour lines. Cellular objects were recognized in a process termed “segmentation”. Recognized objects are presented with color boundaries, within which intensities and other parameters were elaborated.

3.3 Cell culture and differentiation induction

Simpson-Golabi-Behmel syndrome (SGBS) preadipocytes were plated in ibidi 8 well cell culture plates at a density of 15x103 cells/cm^2. Cells were cultured in DMEM-F12 medium containing 10 % FBS, 1 U/ml Penicillin, 1 U/ml Streptomycin, 0.033 µM Biotin, 0.017 µM Panthothen at 37 °C in 5 % CO_2 for 24 hours to become attached. Differentiation was started using the following medium for four days, DMEM-F12 with 1 U/ml Penicillin, 1 U/ml Streptomycin, 0.033 µM Biotin, 0.017 µM Panthothen, 0.1 mg/ml Apo-transferrin (Sigma), 10 µM human Insulin (Sigma), 10 µM Hydrocortisone (Sigma), 20 nM Triiodothyronine (Sigma), 1 mM Rosiglitazone (Caymen Chemicals), 2.5 µM Dexamethasone (Sigma), 25 mM 3-Isobutyl-1-methylxantin (Sigma). Medium was replaced with DMEM-F12 containing 1 U/ml Penicillin, 1 U/ml Streptomycin, 0.033 µM Biotin, 0.017 µM Panthothen, 0.1 mg/ml Apo-Transferrin (Sigma), 10-5 M human Insulin (Sigma), 10-5 M Hydrocortisone (Sigma), 20 nM Triiodo L Thyrosine (Sigma). SGBS cells were stained once with Hoechst 33342 (Hoechst 50 µg/ml, for 60 minutes, washed once), staining solution was then replaced for fresh medium. On the day of measurement, samples were stained with Nile Red (25 µg/ml) and Nile Blue (750 µg/ml) for 20 minutes.

Peripheral blood mononuclear cells (PBMCs) were obtained using Ficoll Paque Plus (GE Healthcare Bio-Sciences AB, Uppsala, Sweden) gradient centrifugation from the peripheral blood of AD patients and healthy controls. mDCs were isolated from PBMCs using the CD1c (BDCA-1)+ Dendritic Cell Isolation Kit (Miltenyi Biotec GmbH, Bergisch Gladbach, Germany) according to the manual. Briefly, after the depletion of CD19+ B cells, CD1c (BDCA-1)+ cells were positively selected. Purified mDCs were then cultured in RPMI-1640 medium (Miltenyi Biotec GmbH) supplemented with 10% FBS (Lonza Group Ltd, Basel, Switzerland) and antibiotics (PAA Laboratories GmbH, Pasching, Austria) for 48 hours in the presence (stimulated) or absence (unstimulated) of 30 ng/ml TSLP (eBioscience Inc., San Diego, CA, USA) and 100 ng/ml SEB (Sigma-Aldrich CO, St Louis, MO, USA).

FRET experiments were carried out using HeLa cells transfected with fluorescent proteins. Membrane proteins of HeLa were stained with Cy5 succinimidyl ester to define cell contours for segmentation of LSC data.

Primary mouse embryonic fibroblasts (PMEFs) were isolated from C57BL/6 13.5 day embryos. 3T3-L1 cells and PMEFs were maintained in Dulbecco's modified Eagle medium (with 4.5 mg/mL glucose), supplemented with 2 mM L-glutamine, 100 µg/mL Streptomycin and 100 IU/mL Penicillin in the presence of 10% Fetal Bovine Serum in 5% CO_2 at 37°C. Two day post-confluence the cells were treated with adipogenic cocktail as described in (49).

3.4 Cell surface marker and intracytoplasmic cytokine staining

Cytokine production by unstimulated and stimulated cells was analyzed after 6 hours of incubation with 3 µg/ml brefeldin A solution to inhibit cytokine secretion. After incubation, the cells were harvested, washed with FACS buffer (phosphate-buffered saline containing 1% bovine serum albumin) and aliquoted into tubes. Cells were first stained with cell surface marker-specific antibodies anti-CD1c-APC (L161, BioLegend, San Diego, CA, USA), anti-CD83-FITC (HB15e, BD, Franklin Lakes, NJ, USA) and anti-CD86-PE (IT2.2, BioLegend) for 30 minutes in the dark at 4°C. The stained cells were then washed with FACS buffer and fixed by adding 100 µl of IC Fixation Buffer (eBioscience) for 20 minutes in the dark at room temperature (RT). Cells were washed with 1x Permeabilisation Buffer (eBioscience), centrifuged, resuspended in 100 µl of 1x Permeabilisation Buffer and stained with various combinations of the following intracellular cytokine-specific antibodies: anti-IL-10-PE (JES3-19F1), anti-IL-2-PerCP-Cy5.5 (MQ1-17H12), anti-IL-4-PerCP-Cy5.5 (MP4-25D2), anti-IL-6-FITC (MAb11), anti-TNFα-PerCP-Cy5.5 (MQ2-13A5) (BioLegend), anti-IL-23p19-PE (23dcdp, eBioscience), anti-IL-12(p40/p70)-FITC (C11.5, BD), anti-TGFβ1-CFS (9016) and anti-CCL17/TARC-PE (54015) (R&D Systems, Minneapolis, MN USA). Cells were incubated in dark at RT for 20 minutes, washed with 1x Permeabilisation Buffer and subsequently with FACS buffer. Cell pellet was resuspended in 30 µl of FACS buffer and loaded into the channels of an ibidi µ-Slide VI (ibidi GmbH, Martinstried, Germany). At measurements, 3 µg/ml DAPI (Sigma-Aldrich) was added for 20 minutes at RT. Unstained cells served as a negative control.

3.5 Plasmid construction, transfection

Construction of the pSV-ECFP-EYFP expression vector (coding for the fusion of the two fluorescent proteins connected by a RNPPVAT linker), serving as a positive control, was described in (50) (Figure 16). Cells co-transfected with ECFP and EYFP plasmids were used as a negative control for FRET. Cells transfected with ECFP or EYFP alone were used for the

determination of spectral cross-talk of the dyes between detection channels. For measurements with LSC, cells were plated in μ-Slide 8-well ibidi coverslips (ibidi GmbH, Planegg/Martinsried, Germany).

3.6 Apoptosis induction

SGBS cells were treated with a mixture of 10-8 M human TNFα (PeproTech) and 10 ng/ml of cyclohexamide (Sigma) for 12 hours to induce apoptosis. Cell death was detected by propidium iodide and FITC-conjugated Annexin V with concentration indicated in Apoptosis Detection Kit (MBL) manual. Samples were washed once with PBS and then kept in fresh medium.

3.7 Halo assay

Each well of ibidi 8-chamber slide was covered by 150 μl of 1 % LMP agarose (Boehringer Mannheim, Indianapolis, IN) melted in 39 °C. The agarose was solidified by placing the slides on ice for 2 minutes. Cells were lysed in ice-cold alkaline lysis buffer [1 % lauryl-sarcosine, 2.5 M NaCl, 10 mM Tris, 100 mM EDTA, 10 % DMSO, 1 % Triton-X-100 (pH 10)] for 10 minutes twice. Slides were neutralized and washed in cold 1x PBS with 5 μM EDTA buffer (pH 7.4) for 4x 4 minutes and fixed in cold 1 % formaldehyde for 4 minutes. The slides were stained with SYBR Gold (Molecular Probes, Eugene, OR) diluted 1:10000 in TE [10 mM Tris (pH 8.0) and 2 mM EDTA] for 15 minutes.

Cellular event before and after lysis was computationally traced object-by-object to associate DNA halo with its original parent cell. Multiple thresholds were applied to analyze SYBR Gold signal, nucleoid matrix was distinguished from migrated DNA in halo ring. Consequently, *Tau*, a parameter monitoring DNA damage, was defined as the fraction of DNA migrated to the periphery of the original nucleus (“halo”) over the total DNA integral of a cell.

3.8 Data acquisition and texture analysis for adipocytes

Laser lines were used in multi-track mode to excite separately fluorophores, namely 405-nm Violet diode laser for Hoechst 33342, 488-nm Argon-ion laser for FITC, Nile Red and propidium iodide, 633-nm HeNe gas laser for Nile Blue. Emission of the sample was collected through an Olympus 40x objective (0.75 NA). Via appropriate emission filters, each PMT determined a specific fluorescent channel, for instance Hoechst was detected at 463±20 nm,

FITC at 530±15 nm, Nile Red at 580±15 nm, propidium iodide and Nile Blue at 675±25 nm. Transmitted laser light was captured by diode photodetectors in which light loss and shaded relief signals were measured to gain information about light absorption, scattering and textural characteristics of the objects.

Texture analysis was done with built-in modules in CellProfiler. Textural parameters were calculated per identified objects. Parameter Entropy measures the randomness of intensity distribution (51): sum entropy (ΣE) roughly informs about the number of lipid droplets. Parameter Variance measures the difference between intensity of the central pixel and its neighborhood (51): sum variance (ΣV) roughly depicts the size of lipid droplets.

3.9 Data acquisition for FRET

A 405-nm solid-state laser, a 488-nm Argon laser and a 633-nm HeNe laser were alternatively operated in multi-track mode to excite ECFP, EYFP, and Cy5, respectively. The autofocus utility determined the inclination of the cover slip by triangulation (based on reflection of the 488-nm laser). During the scan, a fixed offset from the bottom of the cover slip was applied, which placed the focus to the middle plane of cells. Laser intensities at the objective were 151 μW for the 405-nm and 27 μW for the 488-nm lines. Donor and transfer signals with an excitation at 405 nm were collected through 460-500 and 520-580 nm band-pass filters by separate PMTs; the acceptor was excited at 488 nm and detected at 520-580 nm by the same PMT as the transfer signal; Cy5 fluorescence was excited at 633 nm and detected through a 650-nm long-pass filter. Raw scanned images were processed post-acquisition by the CellProfiler software, in which cellular events were defined, and pixel-by-pixel FRET calculations were carried out according to equations described in the section Result 4.3. FRET efficiencies were also calculated on a cell-by-cell basis from the mean cellular intensities gained from the Cell Profiler software by using Microsoft Excel for n~500 cells for each sample. Photostability of the dyes was checked by a time-lapse experiment where the sample was scanned 7 times. The extent of bleaching between two consecutive scans was 1% and 2.8% for ECFP and EYFP, respectively.

4. Results

4.1 High-content analysis of human adipocyte differentiation

Our aim was to quantitate objectively the morphological transition from preadipocytes to adipocytes and their responses to apoptosis induction on cell-by-cell basis with statistical relevance. We have differentiated preadipocytes derived from a patient with Simpson-Golabi-Behmel syndrome (SGBS) into mature adipocytes using a recently developed model for studying human adipocytes with subcutaneous origin (52,53). This cell line has long lasting and high capacity for adipose differentiation displaying a gene expression pattern similar to mature fat cells (54). Cellular responses to apoptosis induction by tumor necrosis factor alpha (TNFα), such as the chromatin aggregation, and uniquely the DNA fragmentation in single cells were also monitored at each differentiating stage.

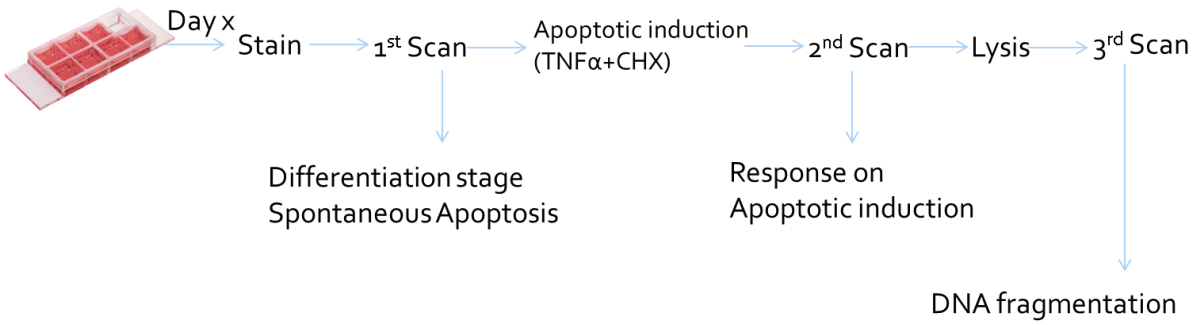

Figure 5. Protocol for high-content analysis of adipocyte differentiation.

4.1.1 Advanced algorithm for high-content data acquisition from human adipocyte cultures

Our principal ambition was to assess cell differentiation in vitro on the single cell level. Thus, a high-content analysis with advanced algorithms was designed and optimized to identify accurately crowded cells in highly confluent adipocyte cultures (47,48). Fluorescent signals from multiple channels were analyzed both in separate and conjoint mode. Hoechst stained nuclei from both cell types (Figure 6a,d) were primarily contoured when the signal exceeded a preset threshold value using *adaptive Otsu threshold* (55). Adipocytes were segmented if fluorescence signals of lipid droplet specific Nile Red (Figure 6b, e) was higher than the background. Image regions occupied by adipocytes were then virtually excluded from further search for preadipocytes. Preadipocytes were subsequently segmented based on the intensity

of phospholipid specific Nile Blue fluorescence (Figure 6c, f). Throughout cell auto-detection, nuclei of cells were firstly identified and marked as *primary* objects (Figure 6d, green contour), based on which the *secondary* objects were later recognized, e.g. associated cell membrane, organelles, or a whole cell (Figure 6e,f, red contour). This two-step process minimized the existence of non-cellular events in data evaluation. We compared our segmentation result to the image partitioning method developed by McDonough (37,38) as well as to ground-truth segmentation by human manual contouring (Table in Figure 6). Accuracy, which is the proportion of the true prediction achieved by the segmentation, and F-measure, which is a more widely used statistical parameter to evaluate imaging algorithms, were calculated. Both parameters ranked our method higher.

Fluorescence intensities of fluorochromes and transmitted light properties inside the contour line were measured and presented as imaging and numerical data including but not limited to: pixel intensities, area (bounded by the contour line in square micrometer), texture of the cell, time of interrogation, and cell location. From these parameters, information regarding lipid accumulation, cell and nuclear size alterations, DNA content and cell phases could be assessed. Additionally, max-pixel fluorescence was used to identify degree of chromatin condensation, particularly when it increased in mitotic or apoptotic cells (23). Analyses of the same cells in cohort type protocols were also carried out by scanning image layers before and after treatments. Subsequently, correlated evaluation of the data was made by merging different layers.

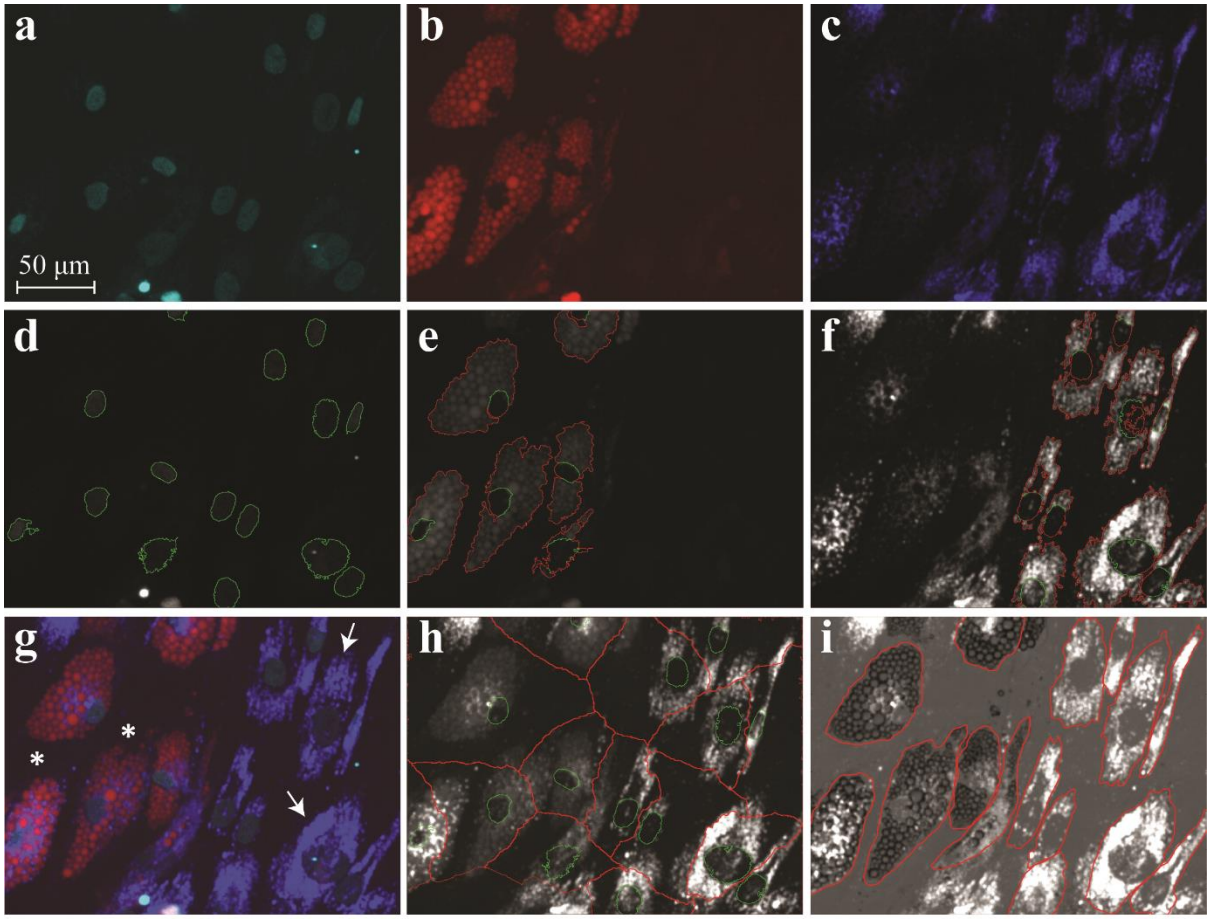

Segmentation		Present work	Partition	Ground-truth
Number of identified objects		15	16	15
	Preadipocytes (with nuclei)	9	9	9
	Adipocytes (with nuclei)	6	6	6
	Non-Cell objects	0	1	0
	Accuracy	100.00%	93.75%	100%
	F-measure	100.00%	94.74%	100%
Area covered by objects		38%	99%	51.41%
	Preadipocytes (with nuclei)	18%	51%	26.40%
	Adipocytes (with nuclei)	20%	43%	25.01%
	Non-Cell objects	0%	5%	0%
	Accuracy	73.92%	51.93%	100%
	F-measure	74.89%	51.24%	100%

Figure 6. Comparison of cell recognition algorithms on a representative image. (a) Cell nuclei stained by Hoechst. (b) Adipocytes stained by Nile Red. (c) Preadipocytes stained by Nile Blue. (d-f) Object identification method presented in the article: nuclei were automatically identified as primary objects, contoured with green lines in (d). Secondary objects as adipocytes and preadipocytes were contoured with red lines in (e) and (f), respectively. (g) A merged image of a, b and c. Arrows show typical preadipocytes, asterisks indicate adipocytes. (h) The result

of the segmentation method developed by McDonough (37,38). (i) Ground-truth segmentation by human manual contouring. Table summarizes identified objects enumerated from the two automated methods and manual segmentation. “Partition” refers to the results obtained by the McDonough segmentation method. Area covered by identified objects is calculated as percentage of the total image. Accuracy, which is the proportion of the true prediction achieved by the segmentation, and F-measure are evaluated.

4.1.2 Inspection of adipocyte differentiation using organelle-specific dyes and texture analysis

The differentiation model was designed and inspected for a period spanning 15 days, during which imaging cytometric assays of live cells cultured in ibidi chamber-slides were performed along two parallel courses of study: either sequential substitutes or longitudinal follow-ups. With the former design, a similarly induced group of fresh SGBS cells was divided into subgroups, which were then placed on separate slides; each subgroup was allowed to grow in incubator until its scheduled daily measurement. On the other design, a particular sample was studied in a cohort pattern where cellular changes were tracked on cell-by-cell basis. Both series served to clarify how cellular morphology and lipid content changes at each time point during the progression of the differentiation.

Number, size, and shape, staining signal intensity of lipid droplets accumulated within each cell were enumerated as subcellular objects (Figure 7). However, for a reason depicted by Figure 8, information of individual lipid droplets (size, number, shape etc.) can only help us to distinguish between cell A and B. Such information is not enough to distinguish between cell A and C, given that both A and C contain same amount of lipid droplets, and lipid droplet size is similar.

We therefore enhanced the assessment of differentiation stages, in which transmitted light texture analyses were performed besides lipid droplet staining. Along the differentiation, characteristic texture was identified in undifferentiated cells (Figure 9a, cell #1), committed differentiating preadipocytes (Figure 9a, cell #2), and terminally differentiated adipocytes (Figure 9a, cell #3). Strong correlation between texture properties and fluorescence from lipid accumulation was found (Figure 9b-e). The increase in texture parameter sum entropy in parallel with lipid droplet accumulation was elucidated during the differentiation from preadipocytes (Figure 9b) to adipocytes (Figure 9c). Preadipocytes showed lower sum entropy

and sum variance of texture compared to adipocytes (Figure 9b, d). Benefiting from these two texture parameters, discrimination between preadipocyte and adipocyte populations was more robust than using only Nile Red fluorescence. All texture parameter alterations mainly originated from cellular roughness and granularity changes (Figure 9a) detected via transmitted (and scatter) light signals.

A complex classification strategy was then developed, relying on Nile Red-staining identified differentiation stages, texture properties of light loss, and nuclear condensation; simultaneously, appropriate gating was confirmed by visual identification of cellular events after relocating them. The combination of the Nile Red and texture signal was used to quantitate lipid accumulation, and cells that contained lipid above a preset threshold value were considered differentiated adipocyte. The ratio of number of adipocytes over the total count of nuclei gave rise to differentiation ratio. This ratio was calculated in a region of at least 100 field images. Consequently, data of at least 1000 gated cells were collected and analyzed in cell-by-cell as well as cell-population bases using statistical softwares (GraphPad Prism and Microsoft Excel).

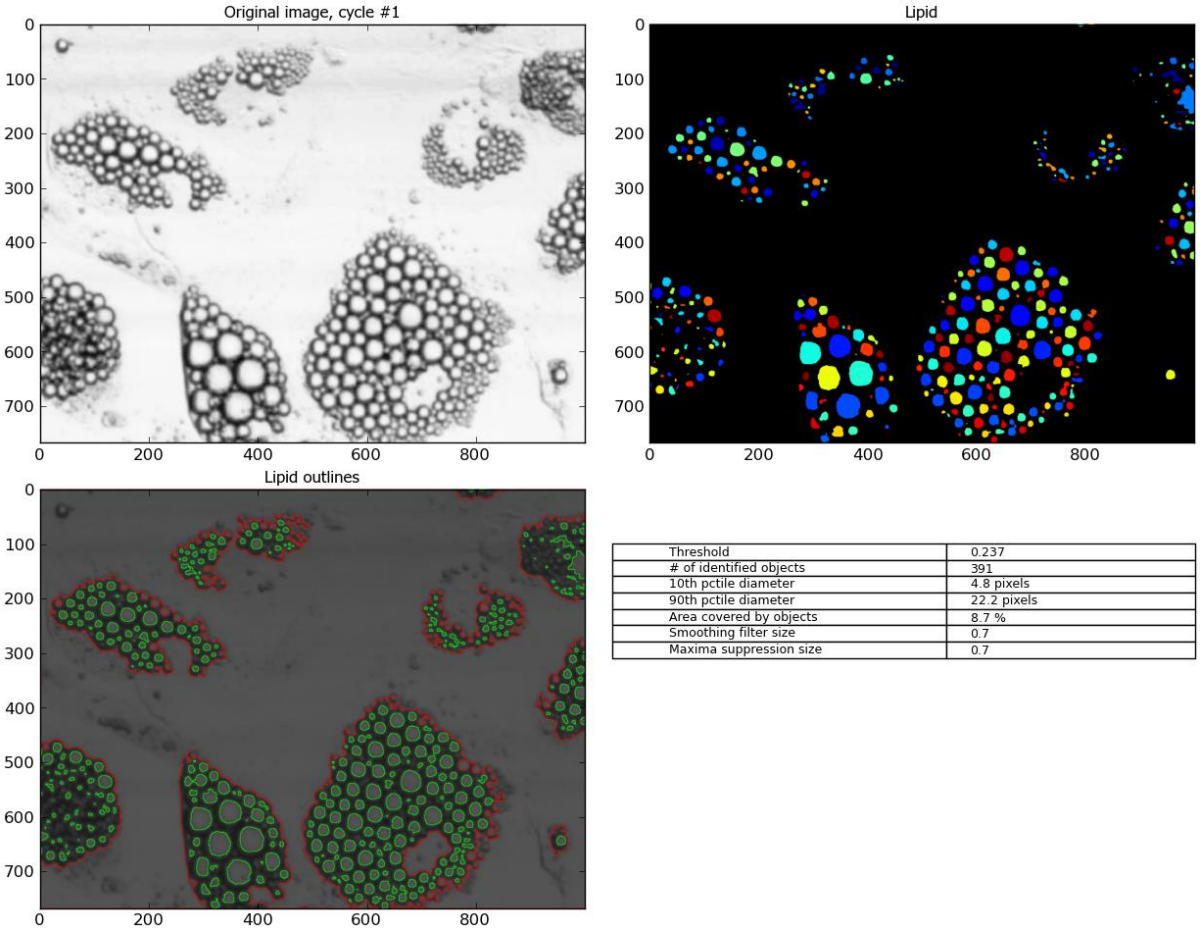

Threshold	0.237
# of identified objects	391
10th pctile diameter	4.8 pixels
90th pctile diameter	22.2 pixels
Area covered by objects	8.7 %
Smoothing filter size	0.7
Maxima suppression size	0.7

Figure 7. Sizing and counting lipid droplet of individual cells.

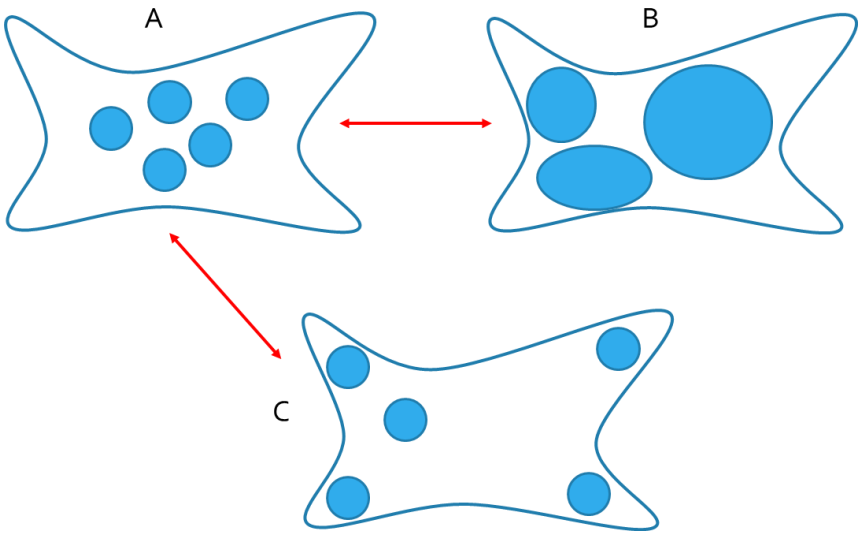

Figure 8. Diagram depicting the variety of lipid contents from cell to cell. The size and number of lipid droplets of cell A and B are completely distinguishable, while that of cell C is completely similar to cell A.

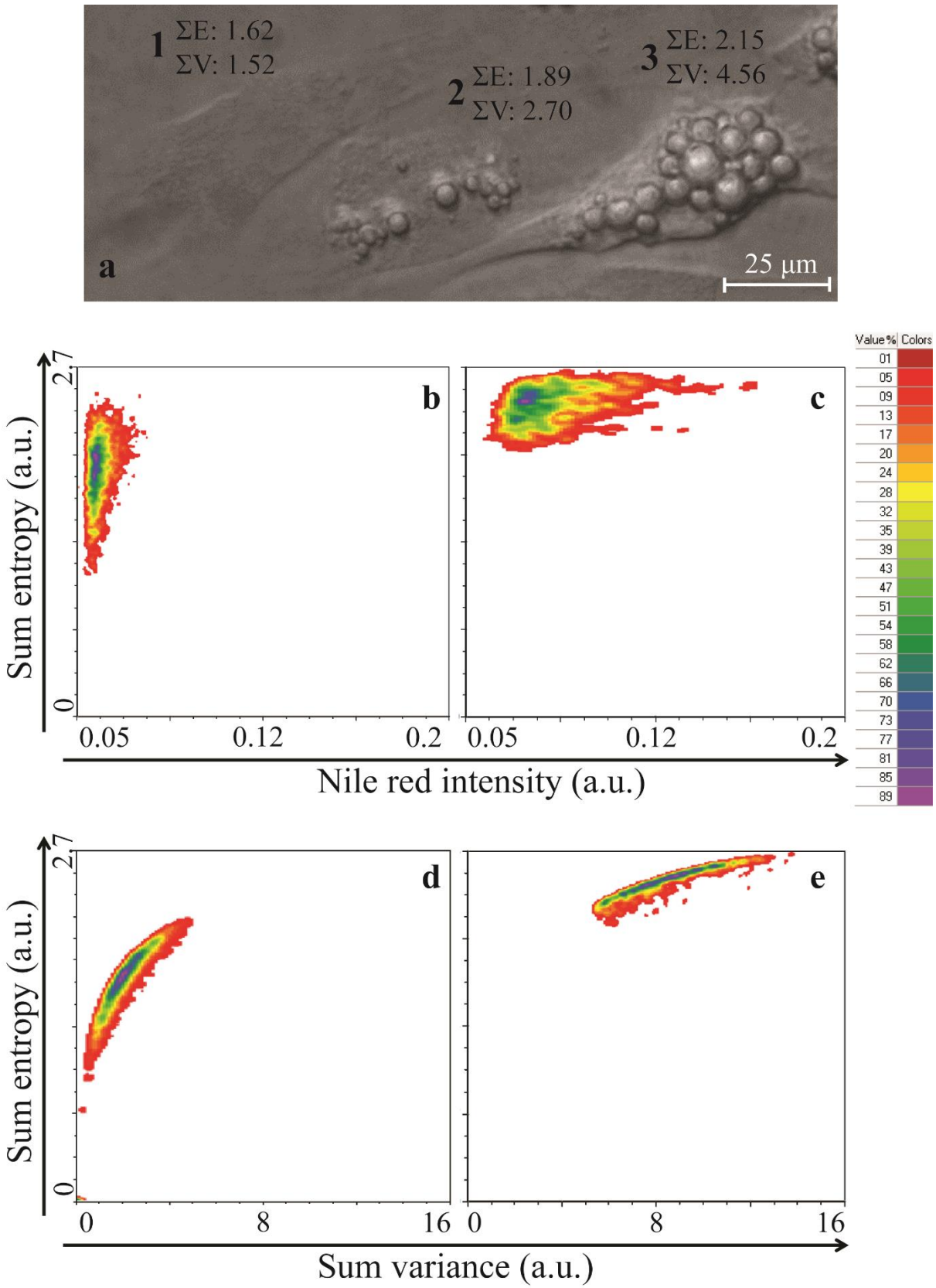

Figure 9. Correlation between texture parameters and lipid specific staining of adipocytes. Texture analysis of light loss signals facilitated cell deciphering. (a) Characteristic texture

patterns of different cell types: object #1 was identified as preadipocyte, while objects #2 and #3 were adipocytes. (b, c) Parameter entropy measured the randomness of the light scatter intensity distribution. The sum of entropy (ΣE) roughly informed about the number of lipid droplets, which was positively correlated with Nile Red staining and both increased during adipocyte differentiation. (d, e) Parameter variance measured the difference between intensity of the central pixel and its neighborhood. The sum of variance (ΣV) roughly depicted the size of lipid droplets and as the cells accumulated more lipid, sum variance increased similarly to sum entropy.

The study of cell differentiation was conducted for 15 days on both cellular and histocytometric aspects. The preadipocyte commitment was found to occur on day 2-3 with a compacting cytoplasm revealed by increasing light-loss signal. At this point, forming lipid structures still did not stain with Nile Red (triglyceride) but only with Nile Blue (phospholipid). Shortly after, day 4-5, minor but measurable Nile Red signal appeared (Figure 9a, object #2). A relatively few small separated lipid droplets and an enhanced nuclear condensation were shown in committed preadipocytes on day 2-5. This was in contrast to undifferentiated cells, which had more cytoplasm, round giant and faintly stained nuclei with no Nile Red fluorescence (Figure 9). From day 6 to day 12 most of the adipocytes reflected typical morphological signs of *in vitro*-differentiated adipose cells, such as round distending shape, a cytoplasm filled with lipid droplets as well as strong Nile Red fluorescence and light-loss signals. Shrinking and more brightly stained nuclei, signs of nuclear condensation, became even more pronounced. At day 9-12, when the ratio of fully differentiated cells reached 40% in the region of optimal confluence (two-dimensional in vitro confluence), the differentiation curve was considered saturated. Indeed, from day 12 until the completion of the experimental regime (18 days), no further formation of lipid droplets was seen, rather the lipid droplets fused together and became distorted.

4.1.3 Detection and quantification of apoptosis in pre-adipocytes and adipocytes

To see the effect of apoptosis induction on differentiating fat cells, spontaneous and induced apoptosis was assessed by a multi-step LSC assay. Before apoptosis induction, a region of interest (ROI) was determined by mosaic scan, where most of adipocytes were located, this region was scanned once to obtain pre-treated control (first scan layer). Next, apoptosis induction was applied and a scan was performed upon same ROI using exactly the same

instrumental setup (second scan layer). Lastly, the sample underwent a halo assay (see Material and methods) where nuclei were examined for DNA fragmentation and a third layer of scan was performed on same ROIs. Merging image data of these three layers gave rise to the correlated data at different experimental phases, i.e. before and after treatments.

On every third day of the differentiation period, apoptosis induction was conducted on preadipocytes and adipocytes using TNFα treatment. Apoptotic ratio was defined as number of Annexin V positive cells over the total count of Hoechst stained nuclei. Before TNFα treatment, Annexin V labeled cells in the first scan layer represented spontaneous apoptosis, whereas AV+ cells in the second scan layer, recorded after the TNFα treatment, indicated the induced apoptosis. Merged first and second layer gave individual information of each particular cell on how it progressed through the apoptosis induction. Images taken before and after apoptosis induction were computationally stacked over each other to allow correlation analyses of cellular information from exactly the same cells before and after the treatment.

We observed a stable spontaneous apoptotic rate in both adipocytes and their precursors, ranging from 7.05 % to 17.91 %. After apoptosis induction, significant increase of Annexin V and propidium iodide positivity were seen in both cell types at every time point of differentiation. Particularly, preadipocytes showed more sensitivity to the apoptosis induction, as 26.06 % to 50.09 % of preadipocytes showed Annexin V positivity compared to that of 30 % average in the adipocyte population.

Additionally, the apoptosis induction brought on apoptotic bodies, which showed highly fragmented DNA in halo assay as well as strong fluorescence of Hoechst intensity. Typical membrane blebs in close association with condensed nuclei were observed in the majority of apoptotic cells. There was remarkable cell loss, which was proportional to the percentage of cells responded to the apoptosis induction: 24.12 % ± 10.5 % of cells was lost in induced samples compared to 10.67 % ± 4.52 % in controls (from data comparing nuclei counts before and after treatment in day-12 samples).

4.2 DNA damage detection in different cell fates and cell lines

With the development and optimization of the single-cell gel (comet) assay in the mid-1980s to early 1990s, DNA damage in individual cells could be examined and quantified with great sensitivity. Cells are embedded in agarose and placed on a slide precoated with agarose, after which they are submersed in a lysis solution, rinsed to remove salt, and exposed to a low voltage. There is little to distinguish the various alkaline lysis methods, which employ a high salt/detergent lysis for a variable period (1 to 24 h), an alkaline rinse or denaturation step (typically 60 minutes), and electrophoresis for about 20 min at a voltage near 0.6 V/cm.

As more breaks are introduced, a measurable fraction of the DNA will begin to migrate. The tail moment is defined as the product of the fraction of DNA in the tail and the distance between the center of mass of the DNA in the tail and that in the head. Thus, with comet assay, the manifestation of DNA breaks is disclosed not only in the distance of DNA migration but also revealed by the discrepancy of fluorescent fractions between the migrated DNA fragments and the intact matrix (Figure 10).

A plausible advantage of the versatile comet assay is that it is able to detect (or be modified to detect) a wide variety of additional types of DNA damage including single-strand breaks, DNA interstrand crosslinks, and base damages that appear as endonuclease-sensitive sites.

However, the comet assay is not suitable for confluent samples, where cells are generally in such close vicinity that the formations of comet of neighbor cells are interfered or overlapped to each other. On the other hand, under certain treatment that could generate large scale of DNA damage, the degree of fragmentation was so great that standard comet measurements by image analysis could not be expressed accurately. Furthermore, using a dedicated image analysis program for comet analysis, the comet measurements were time consuming, thus relatively few events could be measured for each experimental group.

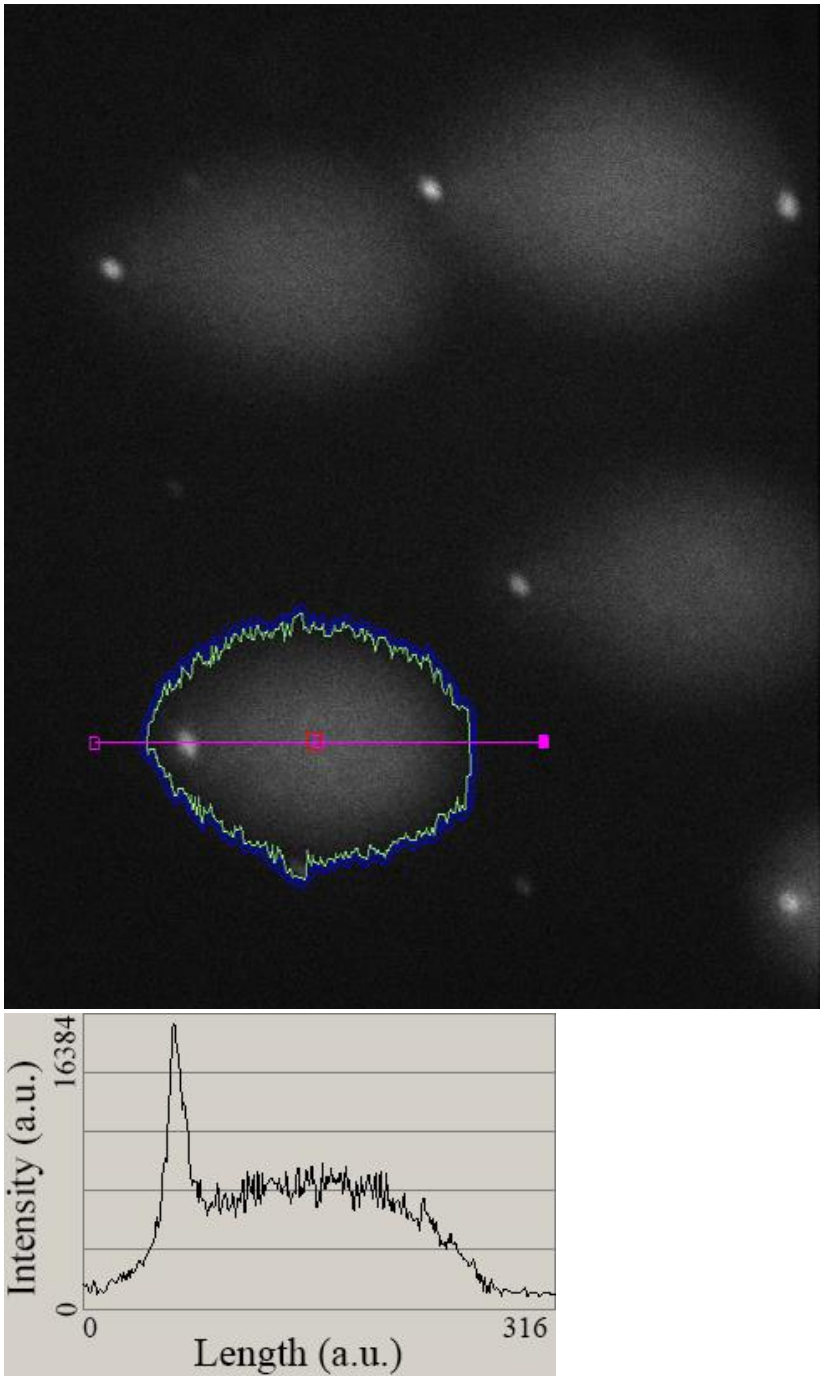

Figure 10. Comet assay on Jurkat cells.

Halo assay

In previous work, we have elaborated a slide-based imaging and flow cytometric method that can perform examination in living cells and give rise unique parameters to identify and correlate DNA damage. This allowed us to determine that the T cells apoptotic DNA damage occurs simultaneously with phosphatidyl serine externalization - an event that is previously thought to occur earlier than the DNA fragmentation (21,56).

Stemming from this methodology, we further developed a screening assay that can systematically examine the level of DNA damage in cells of different tissue origins and under different conditions. We adapted a modification of the comet assay, called the "halo" assay. Using this assay, the damaged DNA forms a halo around the undamaged DNA in the center because the electrophoresis step is omitted. We introduced a new parameter, *Tau*, in order to quantify DNA damage by halo assay using standard LSC software.

$$Tau = \frac{FI_{Halo\ Ring}}{FI_{Total\ Halo}}$$

where $FI_{Halo\ Ring}$ is the integrated fluorescence in the peripheral halo (Figure 12d), $FI_{Total\ Halo}$ is the integrated DNA fluorescence of the matching nucleus (Figure 12b). *Tau* was thus a quantitative entity, linearly proportional to DNA damage (modification of previous study (10)). This allows direct quantification of DNA fragmentation using the parameters collected by the LSC.

4.2.1 Accumulating DNA damage was seen during SGBS adipocyte differentiation

A quantification of nuclear size and shape at population level confirmed that: in preadipocytes, large nuclear size was found to correlate with fainter Hoechst stained DNA (Figure 11a), while adipocytes showed more compact nuclei and brighter Hoechst intensity (Figure 11b). This nuclear condensation lead us to the hypothesis that DNA fragmentation may take place at a certain degree to facilitate such a crucial cellular program as terminal differentiation. Suggestively, other studies in myogenesis have demonstrated that possible involvement of caspase-activated DNAse during cell differentiation. It has also been reported that the lack of caspase 3 activation or dysfunction of CAD stop muscle differentiation, furthermore DNA damage is detected during the otherwise normal process (57).

The DNA detecting assay was thus performed at each inspected time point of differentiation to estimate possible DNA damage.

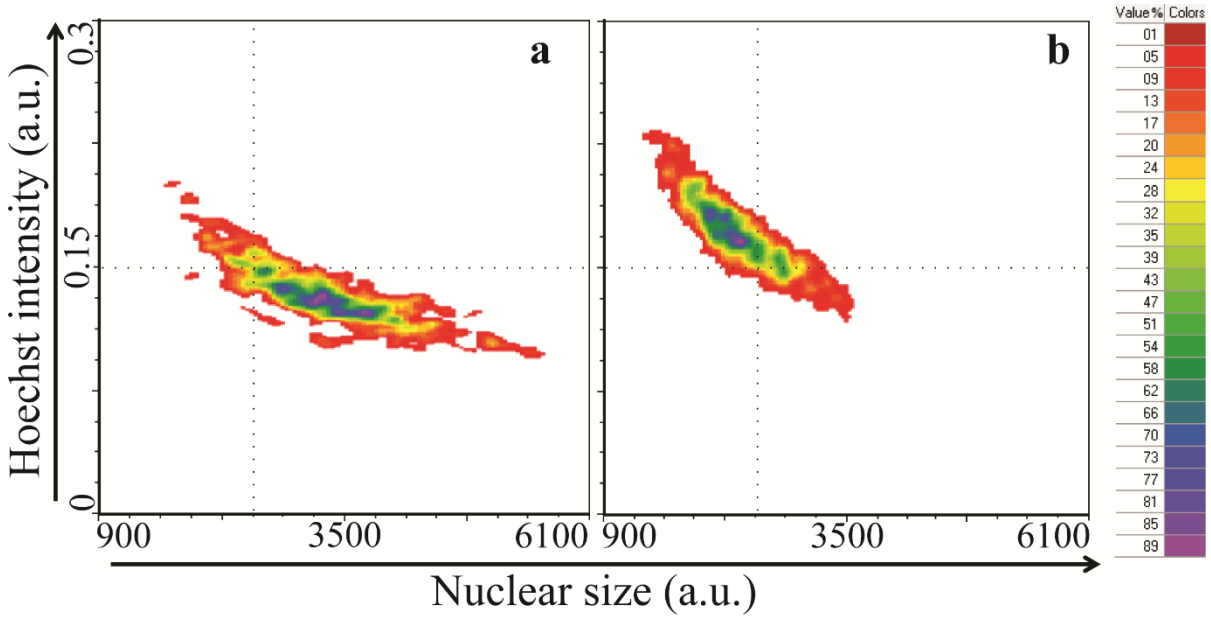

Figure 11. During preadipocyte-adipocyte transition, SGBS cell nuclei become shrunken and their chromatins become more condensed.

Apoptotic cells were identified according to their Annexin V label and *Tau*, a quantitative parameter for DNA damage derived by us (see **3. Materials and Methods**), was calculated in non-apoptotic cells (following alkaline halo assay) at every time point of differentiation.

DNA was stained with SYBR Gold after being lyzed in halo assay. In healthy cells, DNA fluorescence of a halo was confined to the center of nuclei since unfragmented high molecular weight DNA diffuse out at proximal distance (Figure 12a, left structure). In cells that had more DNA damage, smaller fragments migrated further from the central nucleoid matrix (Figure 12a, right structure). Fluorescent signals of total integrated DNA were collected by a lower segmentation threshold in (Figure 12b); whereas fluorescent signals within nucleoid matrix (Figure 12c) were collected by a higher threshold. The halo ring, which was the region between two contoured thresholds, was subsequently segmented (Figure 12d).

There was a strong correlation between high fragmentation of apoptotic DNA and Annexin V positivity, as previously suggested by Bacso et al. (56). Here in our study, we investigated *Tau* on the Annexin V-negative cell population (see 3. Materials and Methods) to elucidate the source of various degree of DNA fragmentation that spontaneously occurred during adipocyte differentiation. As cells differentiated more fully, the *Tau* value rose from 0.16 to 0.27 on day 3, and at day 5 its value plateaued at 0.4, indicating a continuous increase of DNA fragmentation during the differentiation process (Figure 12e). This finding, as an original observation on single cell level, suggests that spontaneous DNA fragmentation occurs during adipocyte differentiation in the absence of apoptosis.

We extend this work for further examination in various differentiating programs of different cell types, namely human and mouse primary cell lines, with both white and brown adipose tissue differentiation protocols.

4.2.2 Accumulating DNA damage was also observed during mouse adipocyte differentiation

To generalize previous finding of DNA damage in other differentiation processes, we inspected the case of DNA damage propagation during adipogenic differentiation in other species, namely mouse adipogenic differentiation, using the conventional mouse 3T3-L1 adipocyte cell line, mouse embryonic stem cells (MESC) and primary mouse embryonic fibroblasts (PMEF) (Figure 13). The confirmative results indeed strengthen and generalize the phenomenon seen in human SGBS cell line. To the best of our knowledge, our work is the first study that reports DNA damage in human adipocyte differentiation.

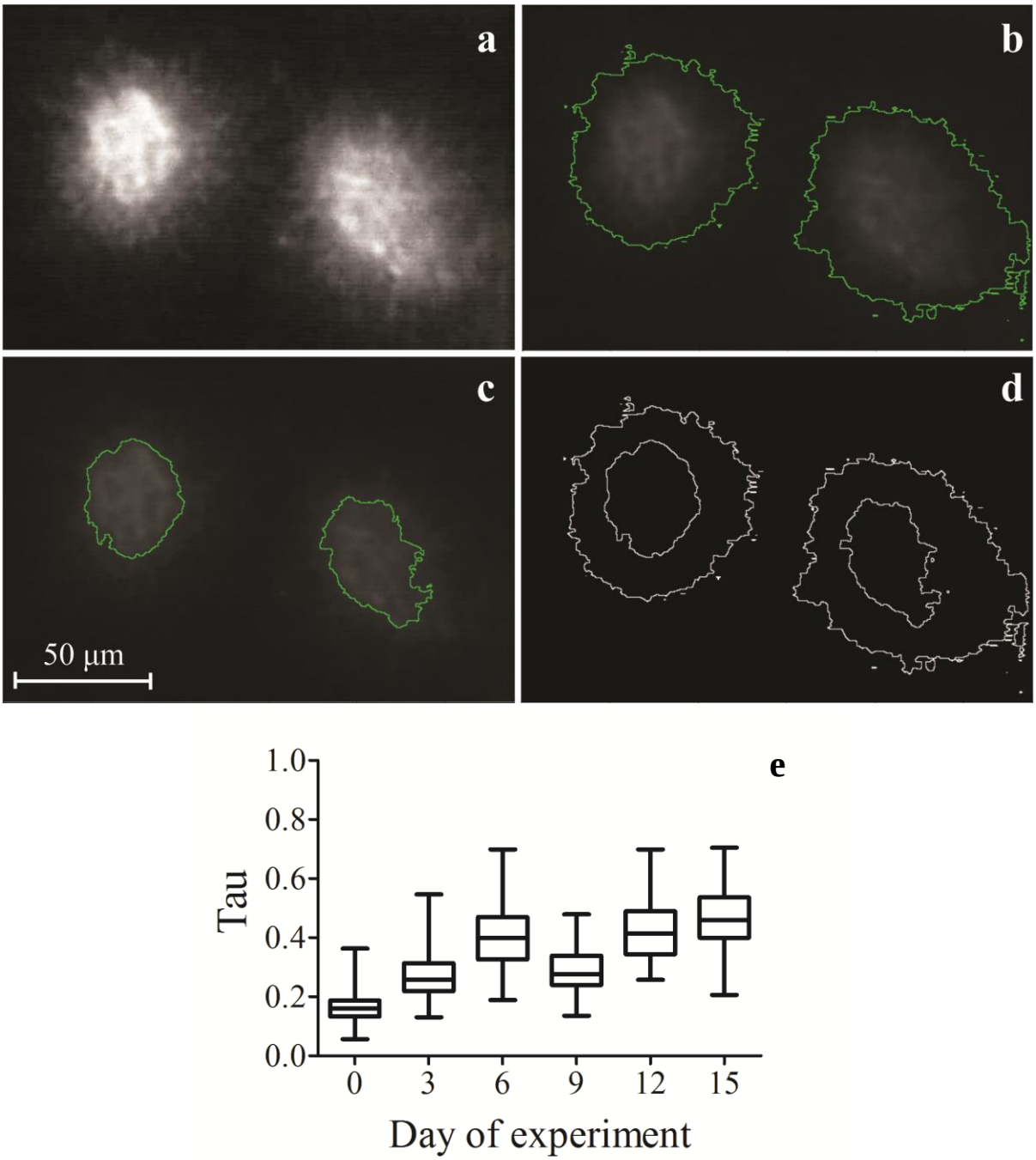

Figure 12. Quantification of DNA integrity. (a)Typical halo formation after lysis is shown after staining DNA with SYBR Gold. Fluorescence of total integrated DNA (contoured in (b)), within nucleoid matrix (c) and within halo ring (region between two grey lines in (d)) were enumerated, respectively. (e) DNA fragmentation accumulated early in differentiating adipocytes. *Tau*, the ratio of migrated DNA in halo over total DNA (halo + matrix), is proportional with degree of DNA fragmentation. *Tau* was calculated from non-apoptotic Annexin V-negative population. From day 0 and 3, data were collected from preadipocytes, while data from day 6 to 15 was collected from maturating adipocytes. At least 150 cells were included each calculation of *Tau*. Box: median, 25^{th} , 75^{th} percentiles, whiskers: full range.

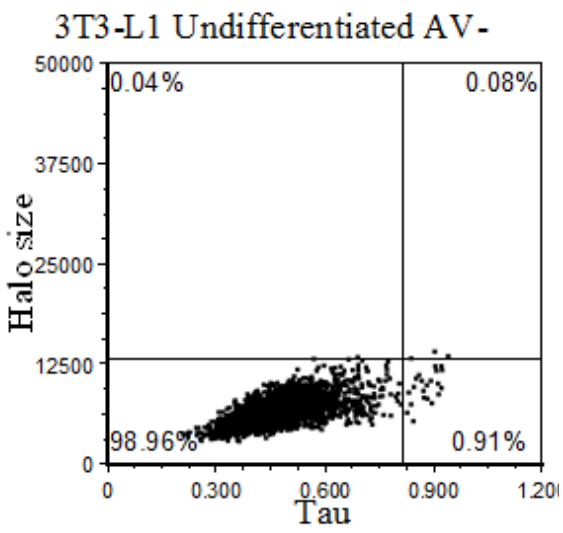
3T3-L1 Undifferentiated AV-
50000
37500
25000
12500
0
Halo size
0.04%
0.08%
98.96%
0.91%
0
0.300
0.600
0.900
Tau

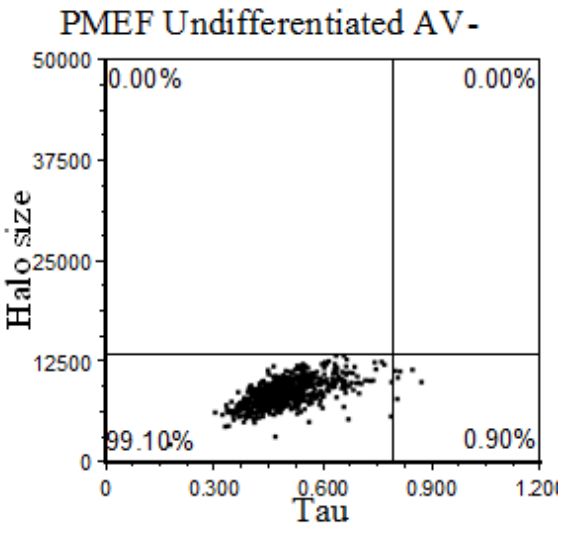
PMEF Undifferentiated AV-
50000
37500
25000
12500
0
Halo size
0.00%
0.00%
99.10%
0.90%
0
0.300
0.600
0.900
Tau

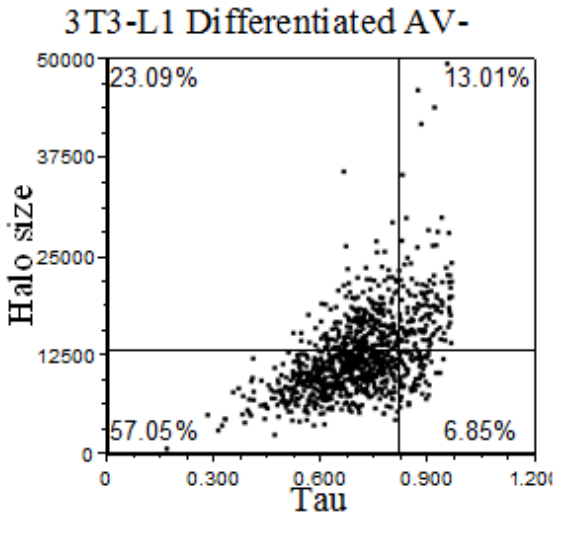
3T3-L1 Differentiated AV-
50000
37500
25000
12500
0
Halo size
23.09%
13.01%
57.05%
6.85%
0
0.300
0.600
0.900
Tau

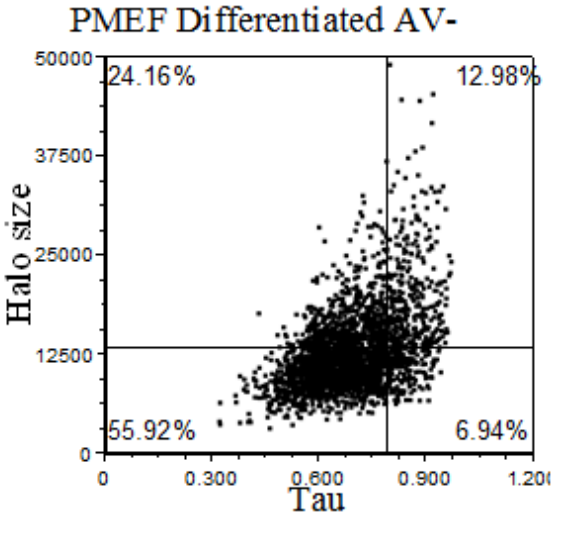
PMEF Differentiated AV-
50000
37500
25000
12500
0
Halo size
24.16%
12.98%
55.92%
6.94%
0
0.300
0.600
0.900
Tau

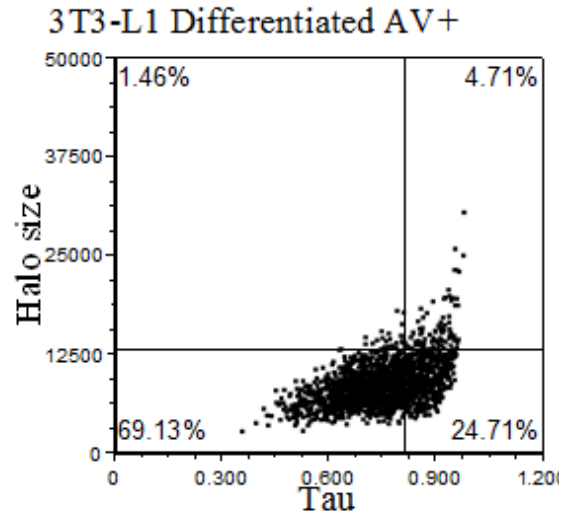
3T3-L1 Differentiated AV+
50000
37500
25000
12500
0
Halo size
1.46%
4.71%
69.13%
24.71%
0
0.300
0.600
0.900
Tau

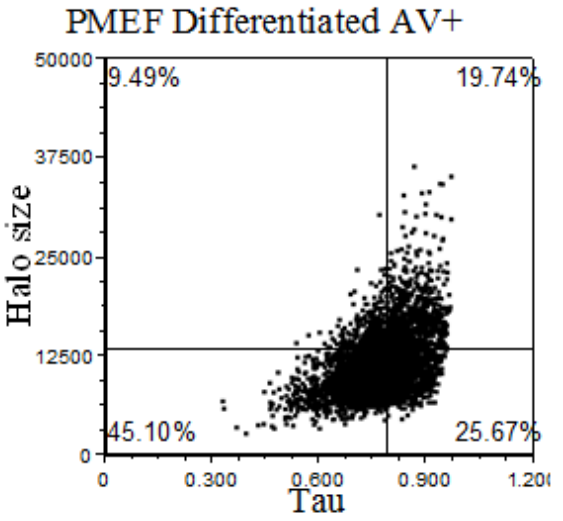
PMEF Differentiated AV+
50000
37500
25000
12500
0
Halo size
9.49%
19.74%
45.10%
25.67%
0
0.300
0.600
0.900
Tau

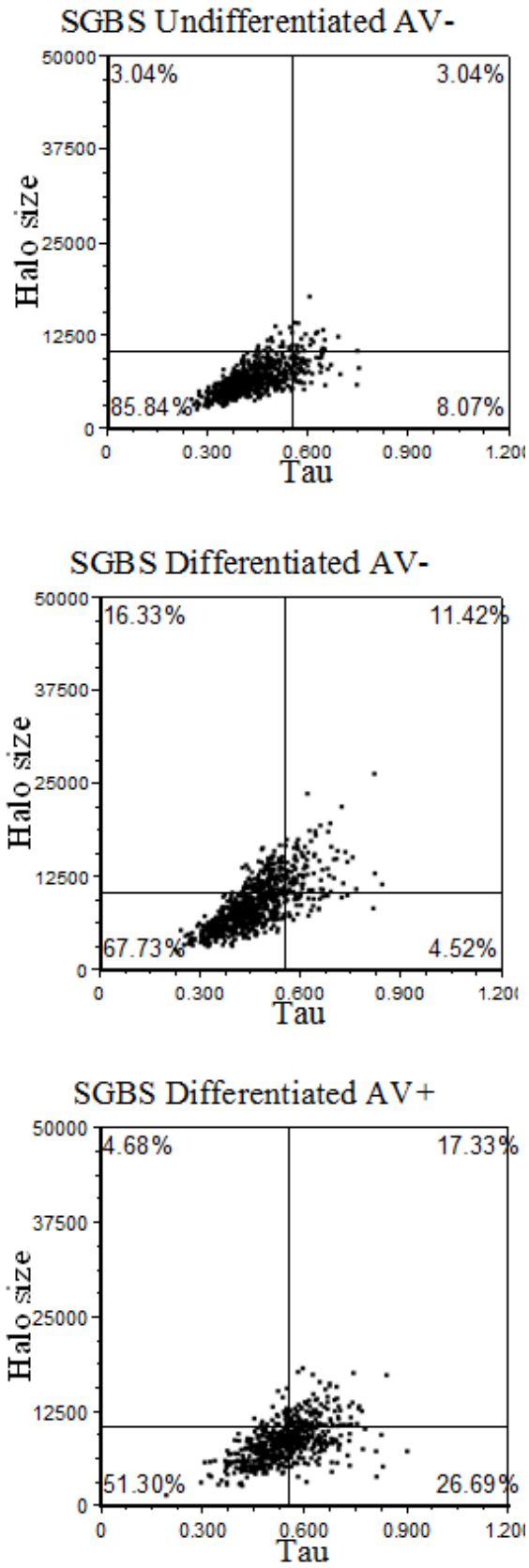

Figure 13. Evidence of DNA damage (high *Tau*) in differentiation processes of various cell lines. Scattergrams show both Annexin V (AV) positive and negative cell population for comparison. Cells with AV(-) are consider non-apoptotic cells.

4.3 Protein-protein interactions as studied by FRET

Fluorescence resonance energy transfer

Fluorescence resonance energy transfer (FRET) is a spectroscopic phenomenon that occurs between two fluorescent molecules: a donor and an acceptor. An excited donor, when it is in an appropriate proximity to a ground state acceptor, transmits its photon energy via a non-radiative mechanism to the acceptor (58) (Figure 14).

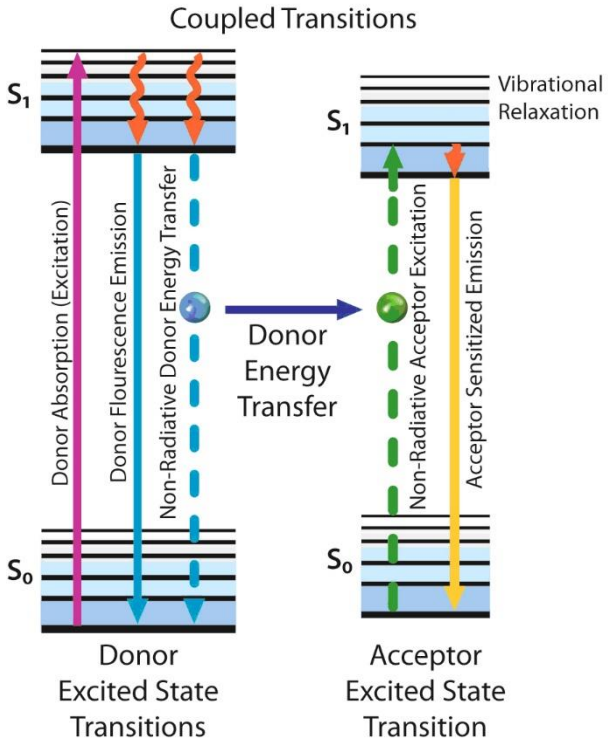

Figure 14. Fluorescence resonance energy transfer (FRET). When two fluorescent molecules are in proximity, FRET happens between the excited state and ground state molecules, if there is an overlap between their emission and absorption spectra (see text).

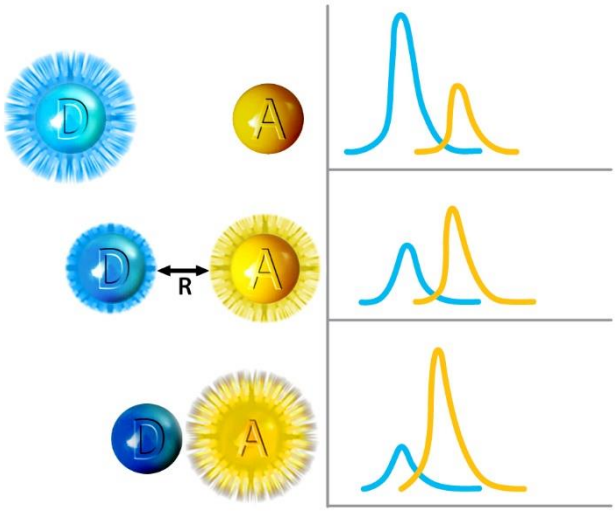

Figure 15. “Spectroscopic ruler”: D: Donor molecule, A: Acceptor molecule; R: distance between donor and acceptor molecules. The left and right panels match in pairs, demonstrating that the closer the distance between the two molecules, the lower the intensity of donor subsides and the higher the intensity of acceptor rises (after energy transfer).

As proposed by Theodor Förster (59), the rate of energy transfer is inversely proportional to the sixth power of the distance between the donor and acceptor. FRET efficiency can be defined as:

$$E = \frac{1}{1 + (r/R_0)^6}$$

Where:

r is the distance between the donor and the acceptor,

R_0 is the Förster distance of this pair of donor and acceptor at which the FRET efficiency is 50%.

Because the energy transfer efficiency is such extremely sensitive to distance changes at molecular proximities, FRET can be utilized as a “spectroscopic ruler” (Figure 15) (60), an excellent tool to obtain structural information in nanometer scale.

Fluorophore candidates for FRET pairs

One of the best-known pair of fluorescent proteins that serve as FRET couple is cyan fluorescent protein (CFP) and yellow fluorescent protein (YFP). CFP and YFP are genetic mutants of the *Aequorea victoria* derived green fluorescent protein (GFP). Both comprised of 238 amino acids (26,9 kDa) and display different spectral properties than the GFP. CFP can be peak excited at 433 nm and it emits at 477 nm maximal wavelengths. It has some disadvantage that it bleaches quickly after being excited, and CFP has a relatively low quantum yield.

The excitation peak of YFP is 515 nm and its emission peak is 530 nm. Excitation of only CFP can result in fluorescence resonance energy transfer (FRET) through a process that a non-radiative energy transmission the energy of the CFP donor is captured by the acceptor YFP, and fluorescence light emission is then generated from the excited YFP. Since YFP is not excited well at the short-wavelength excitation maximum of the CFP, most of the fluorescence detected at the emission wavelength of the YFP, is YFP-specific and it results mainly from FRET (61,62). The spectral overlap of CFP and YFP emission leads to some extent crosstalk between the two signals. This crosstalk should be counted as the FRET background (see FRET evaluation).

Donor photobleaching

Energy transfer efficiency can be measured by selectively bleaching the donor or the acceptor. In donor photobleaching, the time constant of the kinetics of the donor intensity is measured along the laser illumination of donor, which brings photobleaching (63-65). The increased time constant of a potential FRET sample compared to the donor only sample supports the presence of FRET. Transfer efficiency (E) can be calculated by the following simple equation: $E_{Pb} = 1 - \tau_D/\tau_{DA}$, where τ_D is the time constant of the donor (CFP only) sample and τ_{DA} is the time constant of the donor (63) measured in the presence of the acceptor (CFP-YFP fusion sample, Figure 16). The benefit of photobleaching methods is the simplicity of the experiment and data analysis, convenient usage of photo-labile property of CFP, and it gives an opportunity to determine FRET efficiency without α factor, the instrument parameter required to determine ratiometric E. Concurrently, its disadvantage is that it is not high throughput.

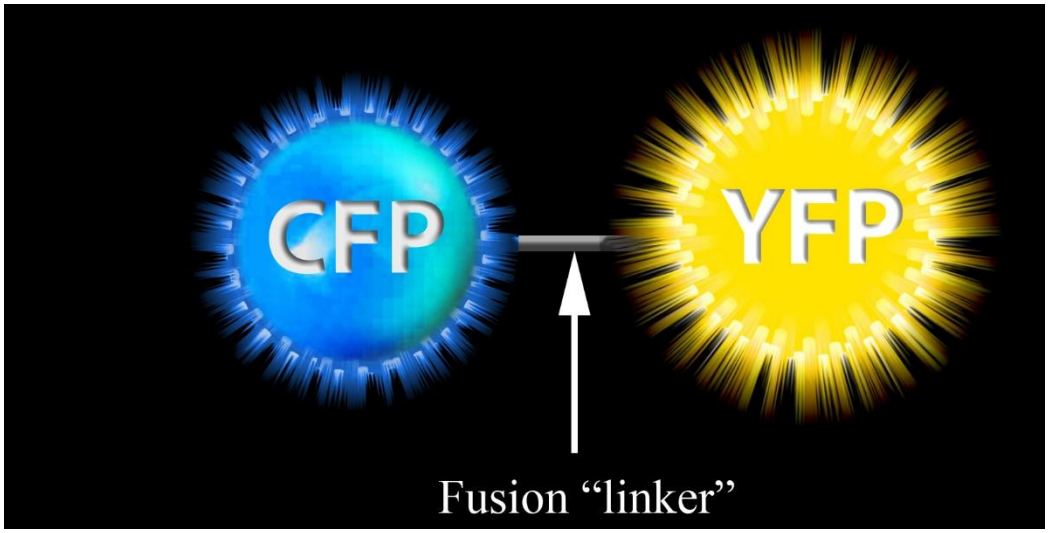

Figure 16. Figure explains the effect of the physical linkers between CFP and YFP in protein constructs. CFP and YFP are held closer to each other with a translated linker in such a distance that facilitates FRET as what was in the “fusion - positive control” sample.

Ratiometric FRET measurement

Contrary to the photobleaching methods, ratiometric measurements are fast and nondestructive (45,65,66). They are based on the simultaneous detection of donor quenching and acceptor sensitization at multiple wavelengths. By using spectral and instrumental correction factors, pure donor and acceptor intensities, which are proportional to the expression levels, and FRET efficiencies can be derived on a cell-by-cell or pixel-by pixel basis by using flow cytometry or imaging microscopy. The flow cytometric version of the method provides excellent statistics over large cell populations, while microscopic imaging allows FRET analysis of adherent cells with sub-cellular resolution and in a repetitive manner in situ.

Application of FRET to investigate protein dimerization

Fos and Jun proteins are members of the bZIP family of transcription factors containing a highly conserved basic region involved in DNA binding and a heptad repeat of leucine residues. They function as homo- or hetero-dimers that bind to AP-1 (activator protein-1) regulatory elements in the promoter and enhancer regions of numerous mammalian genes (67,68). Because of their propensity to form stable heterodimers via a leucine-zipper, Fos and Jun are often used as positive controls in dimerization studies.

Here we demonstrated their stable heterodimer formation by using protein fusion designs, CFP-tagged Fos and YFP-tagged Jun. LSC was used for the identification of FRET in adherent, ECFP-EYFP double-positive HeLa cells.

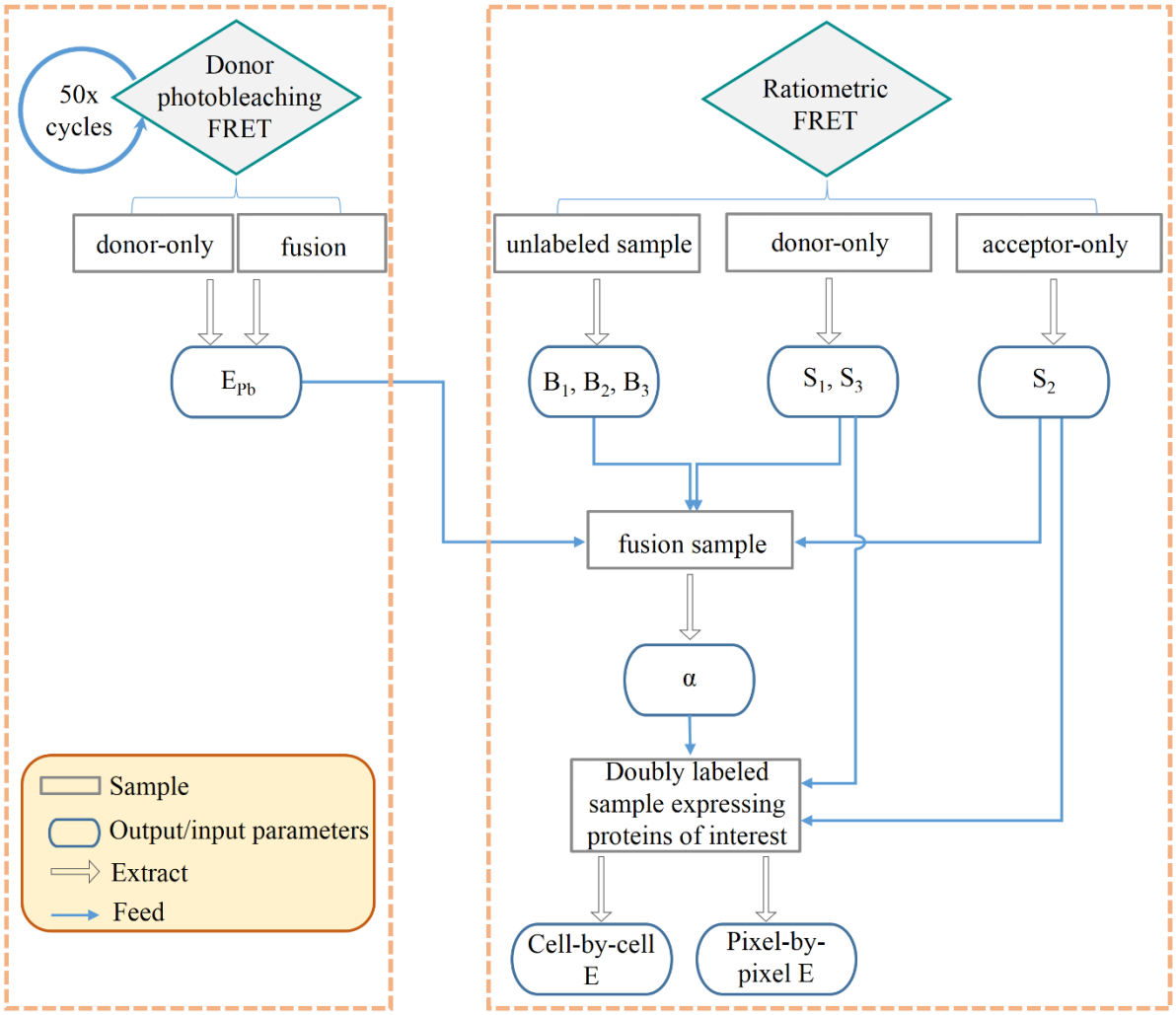

Figure 17. Workflow of FRET efficiency calculations. The diagram represents our computational steps to extract correction factors from control samples and the use of these factors in further calculations to get FRET efficiencies.

To determine the apparent FRET efficiency value (*E*) in a large number of attached cells, we constructed a ratiometric protocol (Figure 17, right side) to be executed in a high throughput fashion. Fluorescence signals were collected in the donor, transfer, and acceptor channels. Ratiometric FRET efficiencies were derived from the signals on a cell-by-cell (Figure

18) or pixel-by pixel basis (Figure 20), where the latter also provided the subcellular visualization of FRET efficiency.

However, FRET efficiency calculation by ratiometric FRET requires the instrumental correction factor α. Therefore, we constructed an additional LSC protocol (Figure 17, left side) to gain E_{Pb} FRET efficiency and derive consequently the correction factor α from E_{Pb}. With gained α, desirable high-throughput ratiometric protocol could be then performed. In this study, we used donor photobleaching instead of acceptor photobleaching because spectral parameters of the ECFP, EYFP, and laser settings of our LSC system are more suitable (405 nm bleaches the donor selectively, but 488 nm bleaches both the acceptor and the donor). The two intertwined protocols provided all necessary parameters for FRET determination and thus gave LSC system an independent capacity to measure protein-protein interaction without the aid from other instruments.

It is essential to include only living cells in evaluation of FRET efficiency. To avoid complication of fluorescent interferences in FRET calculation, we minimized the number of staining dyes and thus did not use specific staining that could discriminate viable and dead cells, i.e. membrane or nuclear staining that is sensitive for detection of apoptotic or necrotic cells. In our protocol, we used the membrane impermeable Cy5 succinimidyl ester fluorescent dye. Cy5 signal was primarily used for recognizing cellular objects (Figure 18a,b). It also helped discriminate live and dead cells based on Cy5 intensity, since Cy5 bonded covalently to primary amine groups of proteins at the cell surface of living cells whilst it penetrated into dead cells (Figure 18d, h). Furthermore, we used cell axial length (Figure 18c) and texture (Figure 18e) as another parameters to exclude unacceptable cells. Adherent HeLa cells usually possess filopodia (Figure 18f), thus have a clear difference between the lengths of the major and minor axes. Floating detached cells obviously featured rounded shape with equal axes (Figure 18g). Cells that had blebbing or ruptured membrane often possessed a more granular texture (Figure 18h).

The calculation of ratiometric FRET efficiencies were adapted from earlier works (69-71). The entities in FRET evaluation included the unquenched donor intensity (I_D), the acceptor intensity without FRET (I_A), the FRET efficiency (E), the spectral crosstalks (S_1-S_3), and fluorescence efficiency instrumental (α) factor, and were described by the following equations for LSC (66):

$$I_1 = I_D(1 - E) \quad (1)$$

$$I_2 = I_D(1 - E)S_1 + I_A S_2 + I_D E\alpha \quad (2)$$

$$I_3 = I_D(1 - E)S_3 + I_A + I_D E\alpha \frac{\varepsilon_4}{S_2} \quad (3)$$

These equations were then solved for the apparent FRET efficiency, *E*:

$$E = \frac{I_2 - I_1 S_1 - I_3 S_2 + I_1 S_2 S_3}{\alpha(1 - \varepsilon_4)I_1 + I_2 - I_1 S_1 - I_3 S_2 + I_1 S_2 S_3} \quad (4)$$

where S_1, S_2, and S_3 were spectral crosstalk between the channels, defined as:

$$S_1 = \frac{I_2}{I_1} \quad (5)$$

$$S_3 = \frac{I_3}{I_1} \quad (6)$$

calculated from a donor-only labeled sample, and

$$S_2 = \frac{I_2}{I_3} \quad (7)$$

calculated from an acceptor-only labeled sample.

The term ε_4 is a ratio of the extinction coefficients of ECFP and EYFP at the wavelengths used for exciting the donor (405 nm) and the acceptor (488 nm):

$$\varepsilon_4 = \frac{\varepsilon_{488}^{ECFP}\varepsilon_{405}^{EYFP}}{\varepsilon_{405}^{ECFP}\varepsilon_{488}^{EYFP}} \quad (8)$$

In our case, ε_4 = 0.00978.

The expression of α was as follows (9):

$$\beta = I_2 - I_1 S_1 - I_3 S_2 + I_1 S_2 S_3$$

$$\alpha = \frac{\frac{\beta}{E} - \beta}{(1 - \varepsilon_4)I_1}$$

The calculations for different factors were explained in more details in (66,72,73).

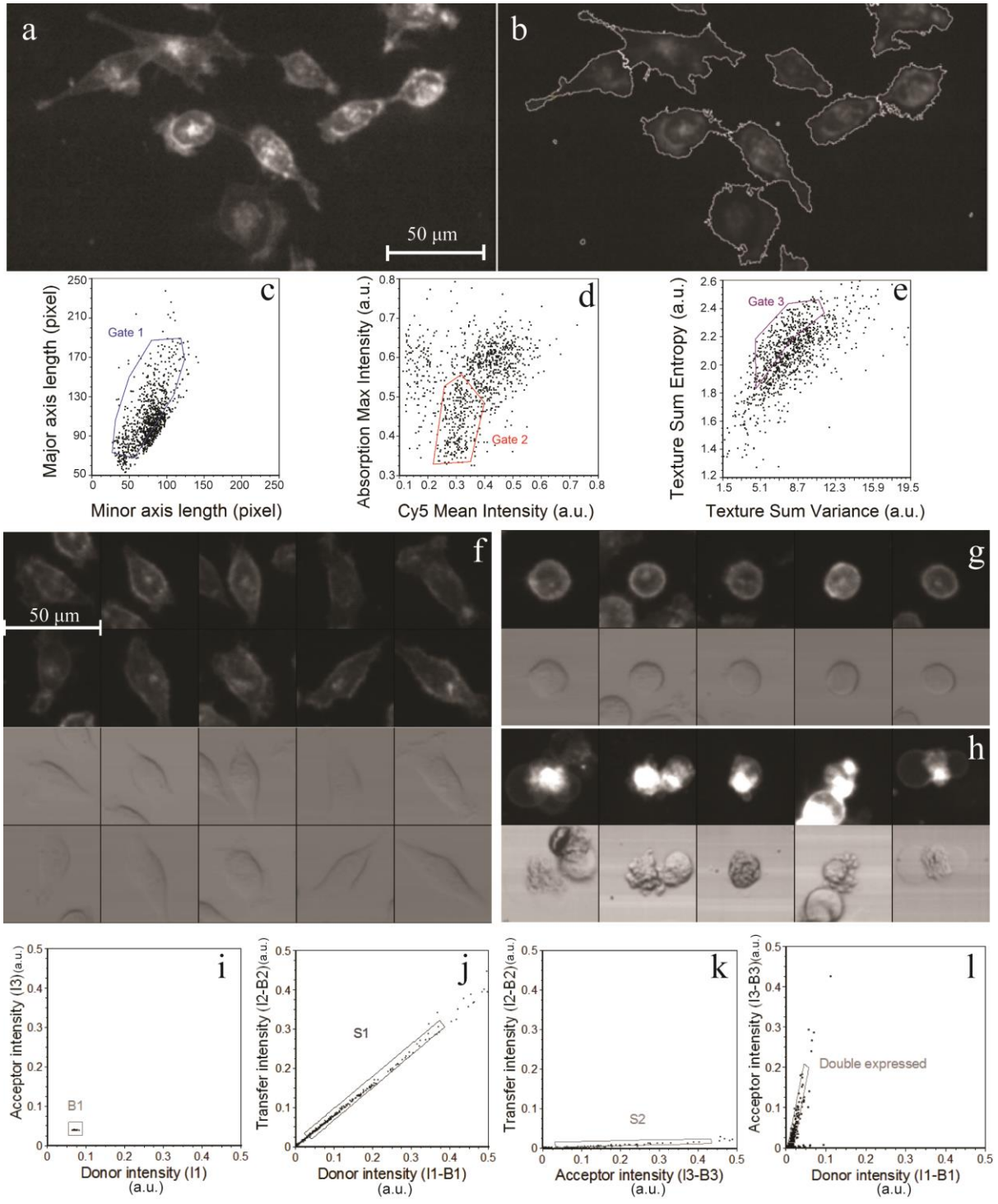

Figure 18. Segmentation and multi-step gating of LSC data. (a), (b): CellProfiler image analysis software was applied, in which Otsu's auto-threshold module was utilized to detect cellular events and declump cell clusters that have distinctive Cy5 signal. Identified events were marked by segmentation contours (grey lines). (c): Adherent cells with elongated processes having a clear difference between the major and minor axes were selected in gate 1. (d): Floating cells having a large absorption signal and dead cells highly permeable to the Cy5 stain were excluded by gate 2. (e): Cells with granular morphology or blebbing membrane

(suggestive of necrotic and apoptotic cells) were excluded by gate 3. (f-h): Galleries of randomly picked cells from the gated population were generated to confirm visually the outcome of the gating procedure. Typical attached (f), floating (g), and dead cells (h) are presented. (i): Background determination was done on single Cy5-labeled cells for auto-fluorescence correction. Cells in gate B1 were selected for determining background intensities of donor and acceptor signals; background of the transfer signal was determined similarly. (j): Background-corrected intensities of donor and transfer signals from the single ECFP-labeled sample were plotted to determine the S1 correction factor. (k): Similarly, transfer vs. acceptor signals from the single EYFP-labeled sample was used to determine S2. (l): From double-labeled samples, cells expressing both donor and acceptor (Fos-ECFP and Jun-EYFP) were selected for FRET evaluation. Highly overexpressing cells were excluded.

In donor photobleaching results, ECFP-EYFP fusion sample showed significantly longer exponential decay of intensity (slower bleaching kinetics) than that of both the ECFP only and the ECFP and EYFP co-transfected sample (Figure 19). This indicated the presence of FRET in fusion sample, reflecting the close molecular proximity of FRET proteins. Energy transfer efficiency for the positive control of ECFP-EYFP fusion sample was ~40%, between 36-52%, when calculated from the measured τ_D and τ_{DA} bleaching time constants. The negative control ECFP and EYFP co-transfected sample remained below 5%, closer to 0%. The positive control also delivered an average *E* value to feed ratiometric equations, by which α factor for the LSC was achieved.

When continuing with ratiometric measurements, the average of *E* for the positive control was close to 40%, while in the negative control around 0%. For the double-transfected sample Fos-CFP+Jun-YFP, *E* above 5% was accepted as significant value of fluorescence energy transfer efficiency. This value reflected the molecular proximity of the donor and acceptor, and thus indicated that the tagging proteins were closer than 10 nm, the critical limit of the FRET. This also offered a good expectancy for the molecular intimacy of the tagged proteins.

With ratiometric FRET, we recognized a subpopulation of cells where Fos and Jun heterodimerized, reflected by a significant *E*; and other subpopulations where Fos-Jun heterodimerization was missing or small. Of note, *E* value measured in a single cell was an average value or an apparent transfer efficiency. It may come from FRET partners with different proximity or from different ratio of the donor and acceptor fluorophores.

We also acquired knowledge about the pixel-by-pixel subcellular distribution of FRET efficiency harnessing ratiometric FRET by LSC (Figure 20). The heterodimerizing Fos-CFP and Jun-YFP was seen to accumulate in the nucleus, where they gave significantly high FRET efficiency, while in the positive control sample (CFP-YFP fusion), high *E* value originated from both the nucleus and the cytoplasm.

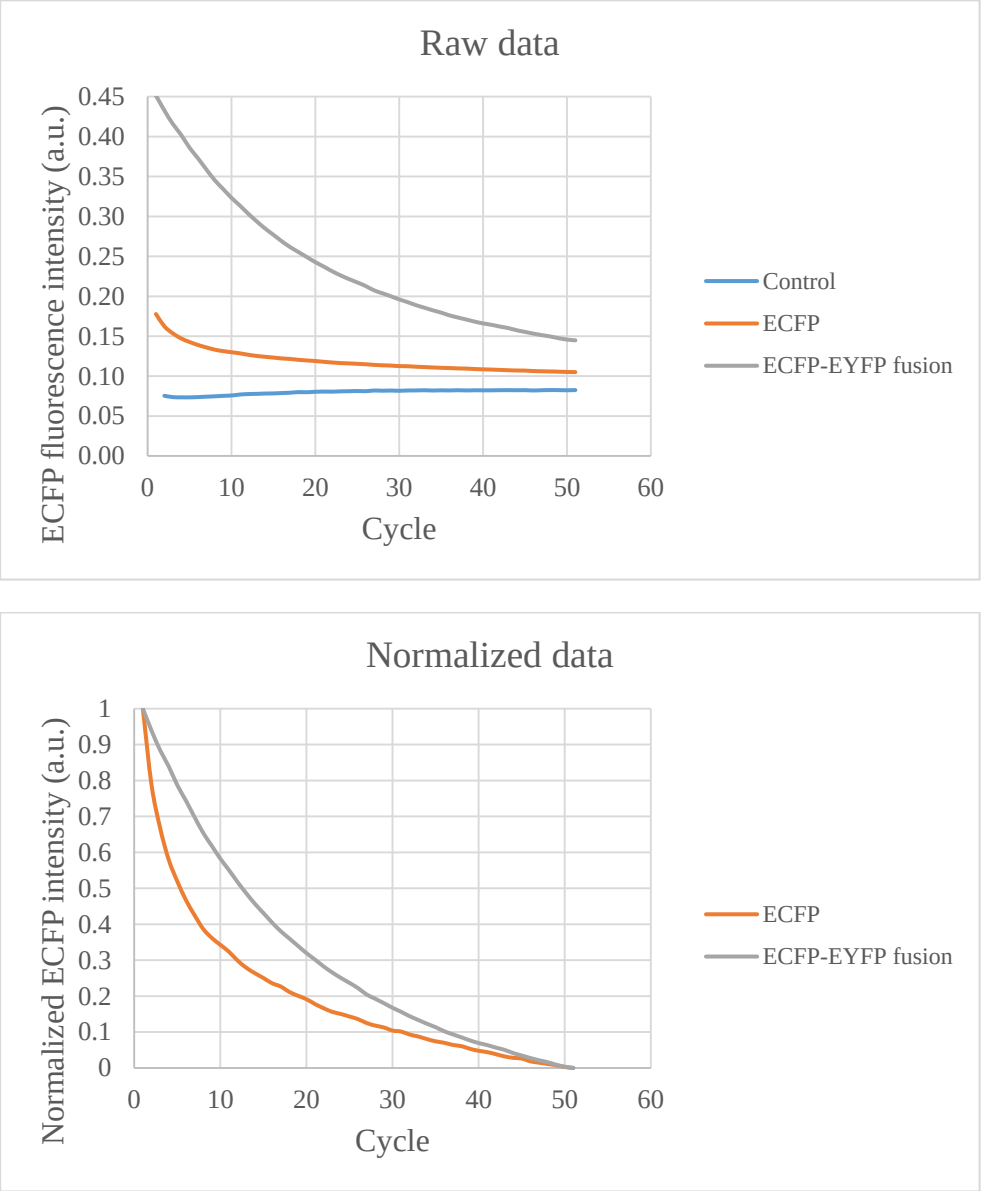

Figure 19. Photobleaching kinetics of fluorescent protein expressing HeLa cells. Representative raw fluorescence intensity (upper) and normalized (lower) donor photobleaching kinetics of cells transfected with ECFP or ECFP-EYFP fusion plasmid constructs. Background is shown only in the upper panel, since after normalization it becomes zero. In the presence of FRET, the bleaching curve of fusion sample is above that of the donor-

only sample, indicating slower bleaching kinetics due to FRET between ECFP and EYFP, and proving their close molecular proximity.

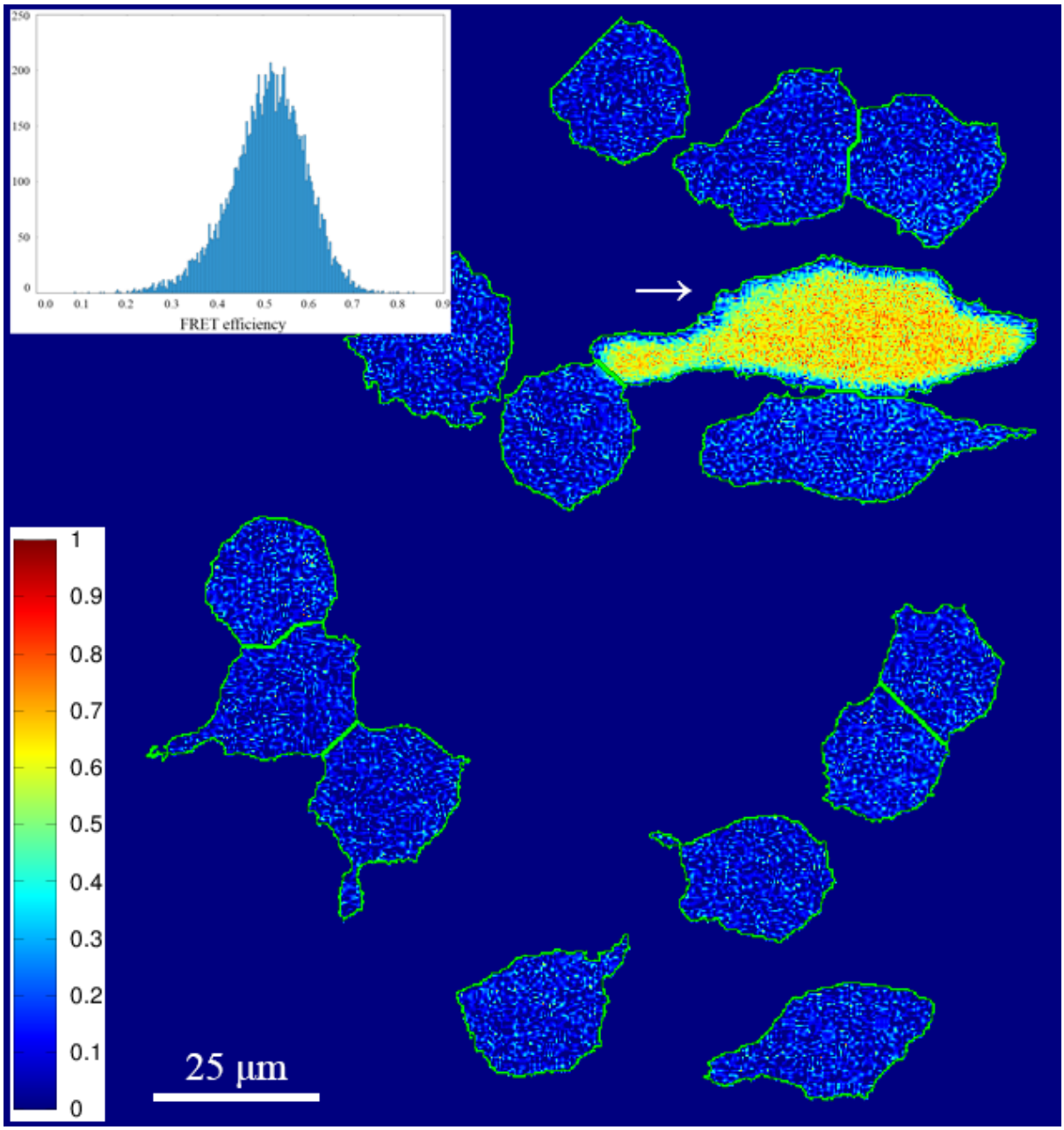

Figure 20. Typical result of pixel-by pixel FRET in color-coded FRET map. FRET efficiency (E) is visualized with a pseudo-color map. In the applied "jet" color scale, pure blue is 0 % and pure red is 100 % FRET efficiency. Green contours indicate identified cellular objects. The figure shows the positive control sample, where the ECFP-EYFP fusion construct was transfected into HeLa cells. This fusion protein lacks nuclear localization sequences, gives a high *E* FRET efficiency value, and is evenly distributed in the one high protein expressor cell indicated by the arrow. The histogram in the upper left corner is the distribution of pixel-by-pixel FRET efficiency in this cell.

4.4 LSC application on studying T helper cell polarization of dendritic cells

In atopic dermatitis (AD), myeloid dendritic cells (mDCs) are actively involved in the initiation and lineage commitment of several skin-infiltrating T helper (Th) subpopulations (74). In turn, mDCs are tightly controlled by tissue microenvironment of the skin (75).

Characteristic features of the skin microenvironment include skin colonization with superantigen-producing Staphylococcus aureus, which correlates with the severity of the disease, and the presence of Staphylococcal enterotoxin B (SEB) and thymic stromal lymphopoietin (TSLP), which is strongly overproduced by keratinocytes in lesional and non-lesional skin due to skin barrier dysfunction (76).

Due to the restricted availability of the clinical samples and limited number of cells per sample from pediatric individuals, we designed our measurement using LSC instead of flow cytometry (11 atopic patients, yielding about 1 million DCs each sampling). The study had been conducted with the major contribution of Department of Dermatology and Department of Dermatological Allergology, University of Debrecen Medical and Health Science Centre, Debrecen, Hungary.

As shown by Nagy et al. (77), the atopic skin-like microenvironment could modulate the T cell-polarizing cytokine production of myeloid DCs. Upon SEB-TSLP dual stimulation, myeloid DCs from AD patients responded by a significant expression of CD83 and CD86 (77). Dendritic cells activated by SEB-TSLP were shown to express cytokines that favor the predominance of Th2 and Th22 subtype.

In AD patients, we reported a high fraction of cells with decondensed chromatin accompanied with increased cytokine expressions. After stimulation, a significant up-regulation of CD83 and CD86 was found, accompanied by further chromatin decondensation, which may imply active transcriptions of dendritic cells (data presented in (77)).

5. Discussion

5.1 Discussion for subsection 4.1- "High content analysis of adipocyte differentiation"

Application of LSC to fat cell analysis

Amongst vast variety of methods to investigate adipocyte biology, genetic approaches, biochemical assays, flow cytometry and conventional microscopy are most commonly used. Although biochemical techniques have largely contributed in understanding adipogenesis and adipoapotosis, it is incomplete to resolve potential heterogeneity of cell populations following a bulk analysis. While common microscopic methods are able to study single cells, their subjective application is user dependent and thus lacks of unbiased quantifications. Flow cytometry has the advantage of being quantitative on single cell level, but it too has inherent shortcomings stemming from its design: handling samples in tubes and lifting cells in suspension.

In our case living adipocytes were cultured in chamber-slides along the entire experiment and measurement; this was especially useful for our follow-up studies of time-resolved differentiation and apoptotic destruction processes. Morphological properties of individual cells as well as stoichiometric data of large populations were inspected and interrogated with minimized perturbation. Plotted data points were also relocated and examined by visualization and thus improved time-lapse experiments with live subjects.

Improved protocol for automated cell segmentation

In slide-based histo-cytometric system, advanced imaging processing is required to enable cell-by-cell analysis in highly confluent samples. When facing this challenge, McDonough et al. (37,38) have introduced tessellation algorithm that could estimate the boundaries between the cells. Still, this procedure would only be valuable when lipid droplets in adipocytes are closely associated with a centric nucleus, which is not always valid since mature adipocytes have typical eccentric nuclei (78,79). On the other hand, tessellation generates pseudo-cell boundaries, i.e. instead of selectively propagating from foreground pixels, the whole image is segmented, and thus collected data would avoidably include also background pixels. In our case, we utilized CellProfiler image analysis software with customizable adaptive Otsu's segmentation and declumping algorithm constituting of two-step

object identification (*primary* and *secondary)*. This protocol has improved cell recognition, cell contouring, and led to a more precise quantitative data acquisition at high cell density of adipocytes. Thus, this work introduced a reproducible and information-rich protocol to follow the differentiation process of preadipocytes to adipocytes from the same SGBS cell population.

Employing texture properties significantly improved adipocyte identification

Beside fluorescent intensity profiles as in conventional imaging microscopy, in this work texture properties of cellular objects were also analyzed and were demonstrated to be an improved approach to investigate morphology of a mixed population of undifferentiated cells, preadipocytes, and white adipocytes.

In flow cytometry, light scatter is generally used for event recognition but forward (FSC) and side scatter (SSC) signals are also valuable parameters to resolve size and granularity of cellular objects. In LSC technology, transmitted light was captured by diode photodetectors in which light loss and shaded relief signals were measured to gain information about light absorption and scattering characteristics of the objects, respectively (80). In LSC, there is no direct side scatter signal, since it would need to be measured in a perpendicular plane, 90^{o} to the projection of forward light beam. Nevertheless, LSC allowed defining several computed texture parameters of image data with absorption and scattering signals, therefore, it was still possible to learn fully of what information might be given flow cytometric side scatter. The computational freedom of texture properties of cells proved to be even more beneficial and gave richer information compared to SSC.

We have used two texture parameters: entropy and variance, which informed us about number and size of formed lipid droplets, respectively. When using these parameters to interpret adipocyte differentiation, we have recognized that these parameters were rather more sensitive or at least give similar results to signals based on conventional fluorescent or chromatic lipid droplet dyes or Nile Red in our instance. In harmony with us, Lee et al. (34) found that side scatter granularity signal in flow cytometry efficiently recognized lipid droplet formation of mature adipocytes differentiated from 3T3-L1 cells. We have broadened their application to slide-based cytometry, where texture parameters provided improved signals for early identification of lipid droplet formation.

Adipogenesis undergoes two stages

The observation that most adipocytes completed terminal differentiation on day 10-12 coincided well with the generally accepted time point when adipocytes were considered fully differentiated. Our results were also in favor of the concept of two stages in adipogenesis: the initial commitment of mesenchymal stem cells to a preadipocyte fate and then terminal differentiation (32). Adipogenic stimuli induced terminal differentiation in committed preadipocytes through the activation of peroxisome proliferator-activated receptor-γ (PPARγ) (32).

5.2 Discussion for subsection 4.2 - "Detection of DNA damage during differentiation"

Nuclear condensation during human adipocyte differentiation

Verstraeten et al. (81) recently showed that level of lamin A and B proteins decreased at peripheral regions of nuclei during adipocyte differentiation, while vimentin reorganized into cage-like structures near lipid droplets. These observations were noted at the same phase of adipocyte transformation identified by us, in which the shrinkage of the size of nuclei along with the increasing intensity of DNA staining were recognized (Figure 11). We suggest that these morphological changes may be the different phenotypical presentations of the same molecular modulation happening together with chromatin condensation.

Increased DNA fragmentation during human adipocyte differentiation

We have observed that *Tau*, indicating level of DNA damage, was continuously increasing from day 3, an early time point even preceding the initiation of texture parameter increase or lipid droplet formation. This is the first time on single cell level, human maturing fat cells are shown to accumulate DNA damage along adipogenesis.

In murine 3T3-T preadipocytes, it was previously shown that DNA repair capacity was reduced during the differentiation program (82-84). However conflicting data has recently risen regarding the repair of double strand breaks in adipocytes, in which a specific DNA repair mechanism for double strand break was shown to be increased (85). Nevertheless, in all of these works DNA damage was monitored in bulk samples, where it was unable to resolve changes on single cell level. Our study introduced, for the first time, the detection of direct DNA damage in single cells during the adipogenesis. Conflicting data mentioned above might

originate from heterogeneous populations with double strand breaks emerging in adipogenesis. These potentially heterogeneous subpopulations might carry different capacity towards various DNA repair routes. This issue might be resolved by our method if direct single and double strand breaks would be measured specifically in single cells.

Accumulation of DNA damage or decrease of capacity of complete replication of genome seems to be a sign of differentiation of somatic cells in multicellular organisms (86-88). In human, for example, red blood cells loose completely their nucleus, platelets are cytoplasmic fragments of megakaryocytes, T and B cells go through DNA editing, peripheral muscle cells form syncytia, and there are many other signs of decreased or specified functionality of the chromatin along the differentiation program.

Caspase 3 has been shown to play an important role in a variety of activation of tissue differentiation (89). It was observed in the differentiation of skeletal muscle, caspase 3 activates CAD, and is linked to the p21 promoter as one crucial step in the normal differentiation. In addition, it has also been reported that the lack of caspase 3 activation or dysfunction of CAD stop muscle differentiation, furthermore DNA damage is detected during the otherwise normal process (57).

Another interesting observation is that FasL and TRAIL- activated apoptosis produce mutagenesis in surviving cells via CAD-mediated effects (90).

We believe that increasing level of average DNA damage we have observed with alkaline halo assay or a possible heterogeneity in developing DNA damage in maturing non-apoptotic SGBS cells is a part of this general phenomenon. We are continuing our work in this field to resolve this possibility.

5.3 Discussion for subsection 4.3 - "High throughput screening of protein-protein interaction"

In this work, a ratiometric FRET protocol specifically designed for laser-scanning cytometry (LSC) was presented. The procedure was aimed to evaluate protein-protein proximities by determining the energy transfer efficiency (*E*) value in large number of attached cells. *E* also provides a quantitative information about protein-protein interactions.

We showed that ECFP and EYFP fluorescence could be detected with sufficiently high sensitivity and accuracy. Application of a reference sample with known FRET efficiency made possible reliable FRET measurements on unknown samples. We compared FRET results obtained with a confocal laser scanning microscope having optimal excitation wavelengths for the excitation of ECFP and EYFP (458 and 514 nm) with results gained from the LSC and a flow cytometer, both having suboptimal excitation wavelengths (405 and 488 nm) (66), (data not shown). By using an ECFP-EYFP fusion protein as a standard, FRET efficiencies measured between Fos and Jun proteins using the different instruments were nearly identical (66).

Furthermore, we have developed a method to measure absolute FRET efficiencies using only the LSC (73). In our scenario, ratiometric measurements required an instrumental correction factor α to determine ahead of the other experiments. We successfully developed a donor photobleaching FRET measurement with LSC to determine *E*, independent from the ratiometric protocol. Using the consensus *E*, this procedure made the determination of α possible.

A limitation of intensity based FRET methods was that they could not resolve donor-acceptor subpopulations characterized by different individual *E* values. The measured apparent *E* value was conventionally an average over individual FRET efficiencies arising from different donors in the cell or in the observation area. Here we demonstrated a solution by using pixel-by-pixel map of FRET efficiencies on a cell-wise measurement.

We defined the methodology for semi-automated FRET measurements uniting the high throughput of cytometric FRET with the capability of subcellular resolution and cell backtracking in a single instrument. Our method can facilitate screening of protein interactions by using FRET-based LSC assays. This high throughput technique provided both statistically

relevant distribution of single cell energy transfer efficiencies in populations and the sub-cellular localization of the pixel-by pixel FRET efficiencies.

5.4 Discussion for subsection 4.4 -"T-helper polarization of dendritics in atopic dermatitis"

We suggest that circulating mDCs have a pluripotent ability to polarize all types of Th cells both in AD and in healthy individuals, but in the presence of the disease specific environmental stimuli, they gain their activated state, which generate characteristic polarizing cytokine patterns secondarily in the skin.

The amount of dendritic cell that could be obtained from clinical patients is generally limited. In this particular study, this limitation is a major obstacle, where the conventional flow cytometric method of investigation is not suitable. Thus, the utilization LSC was proven sufficient to study the effect of new DC-targeted therapeutic modalities in AD.

5.5 General discussion and conclusions

The terms High-Content Imaging and High-Throughput Screening were introduced more than a decade ago (91) and ever since have gained significant momentum due to its ability to study many features simultaneously in complex biological systems (11,92). They define the use of automated microscopy and automated image analytical paradigm to achieve answers for biological questions. Clearly, those technologies are expected to improve significantly phenotypic cellular assays by generating relevant and multi-parametric data sets without laborious works.

From this perspective, our work has been developed based on a laser-scanning cytometry platform. Our presented slide-based demonstrations showed strong capacity to satisfy both unbiased reliability and high-throughput performance. In these works, we utilized the combination of a slide-based scanning platform and image analysis softwares to generate "flow cytometry"-like data, based on the information that is in fact imaging high content data.

This system was capable of being programmed and user can design automated measurements as well as semi-automated analytic procedures, either prior or after measuring the samples. This allowed both automatic acquisition of visual information of cells or tissues and reducing the laborious maneuvers on conventional microscopes.

Analytical companion softwares purchased with the scanning instrumentations usually have restricted capabilities. General options of such default analytical softwares might provide good data mining tools for easy cellular events and objects. They can manage for instance round cells, clearly distinguishable objects, samples with optimal cell density or concentration, tissue sections with homogenous staining, samples with clearly visible and detectable signals, high signal to noise ratio etc. However, each specific study might bring new challenge; for instance: study dealing with cells that require culture in high confluence, cells possessing extensive processes (e.g. filopodia), mobile or dividing cells, cells changing size and shape, and especially hard projects, where we are interested in cellular response to some unpredictable treatments, where features of interest before and after the treatments are required to be recorded and inspected.

Thus, more complex algorithm to facilitate such specific study is largely demanded. Here, we demonstrated our success in developing:

- Multi-step image segmentation to improve cell recognition in heterogeneous, attached cell culture at high confluence.
- Development of texture analysis as a new parameter to study cell morphology and cell differentiation
- Combination of vital and non-vital imaging and analysis to evaluate cell differentiation and concomitant DNA damage.
- Cyclic, time-lapse, and tracking measurement to study protein interactions by FRET.
- Solution to overcome the insufficient procurement of cells in small clinical samples.

We could assess multiple morphological and functional features of both individual cells and cell populations, and the exported stoichiometric data could undergo further mathematical and statistical evaluation procedures. We have shown that our slide-based cytometric approach could make valuable observations in different cell types, cell lines, and treatments. Such achievement on high-content data was based on the detection of total cell signal, where signals were acquired by photomultipliers from the whole depth of the cell, without using confocal pinhole.

Limitations

Performing image analysis for high-content screening requires a strong computational power. Both imaging acquisition, imaging analyzing and data generating processes are time- and resource-consuming, which can restrict multiparametric analysis. This restriction in turn is the main factor that balances between the high-throughput and high-content modality our system. For instance, one fundamental factor affecting the throughput is the time of imaging. When cellular and sub-cellular details are required in high quality, one needs to optimize the exposure time and magnification. Depending on the size and confluence of cells on slide, the size of each viewing field image consequently controls the number of images to acquire per well. This can deeply influence the processing time in a scenario where a large area of the whole 96-well plate is needed to be scanned. The duration of the screening campaign therefore can be too long for living subjects. During such long duration, cells may undergo morphological changes and adversely affect the quality of the scan.

Unfortunately, scanning cytometry also requires a well-trained operator to eliminate the effect of the small physical misalignments that happens during measurements, e.g. when sample holders are replaced, stages are moved, or objectives are changed. Such misalignments can dramatically affect the repetition of automatic cell identification, thus influence assigned analytical values of the investigations.

Further expansion

The implementation of complex assays exploiting primary cells, live cell imaging (time-lapse), cell migration or 3D imaging in a real high-throughput format, is still a tempting goal. In addition, improved analytical systems, "soft-wares", with more precision and automation are indeed drawing more attention than a further improvement of "hardware" instrumentation. Self-learning machine and human-independent analyses have been long a central target of algorithmic studies.

This approach can be potentially expanded to evolve into a more complex and powerful research modality combining gene expression data with cytometric analysis, and quantitative immunohistochemistry with the resolution of organelle specific markers. Once established, such platform would provide scientists an artificial-intelligent advisory system with ready protocols to utilize across many research and health care areas.

6. Summary

The dissertation provides an overview of advancements in high-content screening techniques, with special focus on slide-based imaging cytometry. Contemporary studies that utilized this technology have been highlighted. The review has discussed both the significances, benefits as well as limitations of high-content and high-throughput analyses in different investigations, namely cell cycle analysis, immunophenotyping, quantitative histo-cyto-pathology, cell health analysis, and pharmacology/toxicology.

In addition to the review sections, the thesis has also demonstrated four studies that were conducted by the author and his collaborations: High-content analysis of adipocyte differentiation; High-throughput screening of protein-protein interactions; Detection of DNA damage in differentiating cells; and Study of polarization signaling pathway in dendritics.

These studies exemplified the successful adoptions of laser scanning cytometry into studying cell biology. Moreover, these studies have shown valuable results with both methodological and biological significance. Namely, the author has shown improved cell recognition in heterogeneous, attached cell culture at high confluence; the valuable application of textural analysis in inspection of cellular morphology; pixel-by-pixel FRET map of protein heterodimerization in large number of attached cells; and proofs of the accumulation of low-grade DNA damage during cell differentiation.

The demonstrated applications belong to various orientations and are indeed excellent representatives of objective quantitative cytometry. The establishment of such useful screening platform of the workgroup is encouraging and of great potential, which can effectively serve multiple purposes across different research fields in biology and health cares.

7. References

1. Kamentsky LA. Cytology automation. Adv Biol Med Phys 1973;14:93-161.
2. Kelley KA. Sample station modification providing on-line reagent addition and reduced sample transit time for flow cytometers. Cytometry 1989;10:796-800.
3. Lindberg W, Ruzicka J, Christian GD. Flow injection cytometry: a new approach for sample and solution handling in flow cytometry. Cytometry 1993;14:230-6.
4. Abu-Absi NR, Zamamiri A, Kacmar J, Balogh SJ, Srienc F. Automated flow cytometry for acquisition of time-dependent population data. Cytometry A 2003;51:87-96.
5. Headland SE, Jones HR, D'Sa AS, Perretti M, Norling LV. Cutting-edge analysis of extracellular microparticles using ImageStream(X) imaging flow cytometry. Sci Rep 2014;4:5237.
6. Zuba-Surma EK, Ratajczak MZ. Analytical capabilities of the ImageStream cytometer. Methods Cell Biol 2011;102:207-30.
7. Gest H. The discovery of microorganisms by Robert Hooke and Antoni Van Leeuwenhoek, fellows of the Royal Society. Notes Rec R Soc Lond 2004;58:187-201.
8. Shaner NC, Patterson GH, Davidson MW. Advances in fluorescent protein technology. J Cell Sci 2007;120:4247-60.
9. Nagy P, Vamosi G, Bodnar A, Lockett SJ, Szollosi J. Intensity-based energy transfer measurements in digital imaging microscopy. Eur Biophys J 1998;27:377-89.
10. Pozarowski P, Holden E, Darzynkiewicz Z. Laser scanning cytometry: principles and applications-an update. Methods Mol Biol 2013;931:187-212.
11. Buchser W, Collins M, Garyantes T, Guha R, Haney S, Lemmon V, Li Z, Trask OJ. Assay Development Guidelines for Image-Based High Content Screening, High Content Analysis and High Content Imaging. In: Sittampalam GS, Coussens NP, Nelson H, Arkin M, Auld D, Austin C, Bejcek B, Glicksman M, Inglese J, Lemmon V and others, editors. Assay Guidance Manual. Bethesda (MD); 2004.
12. LoBiondo J, Abramowitz M, Friedman MM. Microscope objectives. Curr Protoc Cytom 2011;Chapter 2:Unit2 2.
13. Negrean A, Mansvelder HD. Optimal lens design and use in laser-scanning microscopy. Biomed Opt Express 2014;5:1588-609.
14. Murray JM, Appleton PL, Swedlow JR, Waters JC. Evaluating performance in three-dimensional fluorescence microscopy. J Microsc 2007;228:390-405.
15. Pawley JB. Handbook of biological confocal microscopy. New York, NY: Springer; 2006. xxviii, 985 p. p.
16. Zhang XD. A pair of new statistical parameters for quality control in RNA interference high-throughput screening assays. Genomics 2007;89:552-61.
17. Zhang JH, Chung TD, Oldenburg KR. A Simple Statistical Parameter for Use in Evaluation and Validation of High Throughput Screening Assays. J Biomol Screen 1999;4:67-73.
18. Zhang XD. A new method with flexible and balanced control of false negatives and false positives for hit selection in RNA interference high-throughput screening assays. J Biomol Screen 2007;12:645-55.
19. Darzynkiewicz Z, Bedner E, Li X, Gorczyca W, Melamed MR. Laser-scanning cytometry: A new instrumentation with many applications. Exp Cell Res 1999;249:1-12.
20. Henriksen M, Miller B, Newmark J, Al-Kofahi Y, Holden E. Laser scanning cytometry and its applications: a pioneering technology in the field of quantitative imaging cytometry. Methods Cell Biol 2011;102:161-205.
21. Bacso Z, Eliason JF. Measurement of DNA damage associated with apoptosis by laser scanning cytometry. Cytometry 2001;45:180-6.
22. Henriksen M. Quantitative imaging cytometry: instrumentation of choice for automated cellular and tissue analysis. Nature Methods 2010;7:243-330.

23. Darzynkiewicz Z, Halicka HD, Zhao H. Analysis of cellular DNA content by flow and laser scanning cytometry. Adv Exp Med Biol 2010;676:137-47.
24. Al-Za'abi AM, Geddie WB, Boerner SL. Equivalence of laser scanning cytometric and flow cytometric immunophenotyping of lymphoid lesions in cytologic samples. Am J Clin Pathol 2008;129:780-5.
25. Tarnok A, Gerstner AO. Clinical applications of laser scanning cytometry. Cytometry 2002;50:133-43.
26. Peterson RA, Krull DL, Butler L. Applications of laser scanning cytometry in immunohistochemistry and routine histopathology. Toxicol Pathol 2008;36:117-32.
27. Nombela-Arrieta C, Pivarnik G, Winkel B, Canty KJ, Harley B, Mahoney JE, Park SY, Lu J, Protopopov A, Silberstein LE. Quantitative imaging of haematopoietic stem and progenitor cell localization and hypoxic status in the bone marrow microenvironment. Nat Cell Biol 2013;15:533-43.
28. Darzynkiewicz Z, Bedner E. Analysis of apoptotic cells by flow and laser scanning cytometry. Methods Enzymol 2000;322:18-39.
29. Darzynkiewicz Z, Huang X, Okafuji M. Detection of DNA strand breaks by flow and laser scanning cytometry in studies of apoptosis and cell proliferation (DNA replication). Methods Mol Biol 2006;314:81-93.
30. Swinney DC. Phenotypic vs. target-based drug discovery for first-in-class medicines. Clin Pharmacol Ther 2013;93:299-301.
31. Ahima RS. Adipose tissue as an endocrine organ. Obesity (Silver Spring) 2006;14 Suppl 5:242S-249S.
32. Cristancho AG, Lazar MA. Forming functional fat: a growing understanding of adipocyte differentiation. Nat Rev Mol Cell Biol 2011;12:722-34.
33. Lowe CE, O'Rahilly S, Rochford JJ. Adipogenesis at a glance. J Cell Sci 2011;124:2681-6.
34. Lee YH, Chen SY, Wiesner RJ, Huang YF. Simple flow cytometric method used to assess lipid accumulation in fat cells. J Lipid Res 2004;45:1162-7.
35. Lin J, Della-Fera MA, Baile CA. Green tea polyphenol epigallocatechin gallate inhibits adipogenesis and induces apoptosis in 3T3-L1 adipocytes. Obes Res 2005;13:982-90.
36. Lin J, Page KA, Della-Fera MA, Baile CA. Evaluation of adipocyte apoptosis by laser scanning cytometry. Int J Obes Relat Metab Disord 2004;28:1535-40.
37. McDonough PM, Agustin RM, Ingermanson RS, Loy PA, Buehrer BM, Nicoll JB, Prigozhina NL, Mikic I, Price JH. Quantification of lipid droplets and associated proteins in cellular models of obesity via high-content/high-throughput microscopy and automated image analysis. Assay Drug Dev Technol 2009;7:440-60.
38. McDonough PM, Ingermanson RS, Loy PA, Koon ED, Whittaker R, Laris CA, Hilton JM, Nicoll JB, Buehrer BM, Price JH. Quantification of hormone sensitive lipase phosphorylation and colocalization with lipid droplets in murine 3T3L1 and human subcutaneous adipocytes via automated digital microscopy and high-content analysis. Assay Drug Dev Technol 2011;9:262-80.
39. Linehan C, Gupta S, Samali A, O'Connor L. Bisphenol A-mediated suppression of LPL gene expression inhibits triglyceride accumulation during adipogenic differentiation of human adult stem cells. PLoS One 2012;7:e36109.
40. Bedner E, Melamed MR, Darzynkiewicz Z. Enzyme kinetic reactions and fluorochrome uptake rates measured in individual cells by laser scanning cytometry. Cytometry 1998;33:1-9.
41. Kwon J. A new approach for the analysis of testicular cells using a laser scanning cytometer. Experimental Animals 2006;55:483-486.
42. Mital J, Schwarz J, Taatjes DJ, Ward GE. Laser scanning cytometer-based assays for measuring host cell attachment and invasion by the human pathogen Toxoplasma gondii. Cytometry Part A 2006;69:13-19.
43. Doan MX, Sarvari AK, Fischer-Posovszky P, Wabitsch M, Balajthy Z, Fesus L, Bacso Z. High content analysis of differentiation and cell death in human adipocytes. Cytometry A 2013.

44. Karpova T, McNally JG. Detecting protein-protein interactions with CFP-YFP FRET by acceptor photobleaching. Curr Protoc Cytom 2006;Chapter 12:Unit12 7.
45. Vereb G, Nagy P, Szollosi J. Flow cytometric FRET analysis of protein interaction. Methods Mol Biol 2011;699:371-92.
46. Leuchowius KJ, Weibrecht I, Landegren U, Gedda L, Soderberg O. Flow cytometric in situ proximity ligation analyses of protein interactions and post-translational modification of the epidermal growth factor receptor family. Cytometry A 2009;75:833-9.
47. Carpenter AE, Jones TR, Lamprecht MR, Clarke C, Kang IH, Friman O, Guertin DA, Chang JH, Lindquist RA, Moffat J and others. CellProfiler: image analysis software for identifying and quantifying cell phenotypes. Genome Biol 2006;7:R100.
48. Kamentsky L, Jones TR, Fraser A, Bray MA, Logan DJ, Madden KL, Ljosa V, Rueden C, Eliceiri KW, Carpenter AE. Improved structure, function and compatibility for CellProfiler: modular high-throughput image analysis software. Bioinformatics 2011;27:1179-80.
49. Cuaranta-Monroy I, Simandi Z, Kolostyak Z, Doan-Xuan QM, Poliska S, Horvath A, Nagy G, Bacso Z, Nagy L. Highly efficient differentiation of embryonic stem cells into adipocytes by ascorbic acid. Stem Cell Res 2014;13:88-97.
50. Baudendistel M, Müller G, Waldeck W, Angel P, Langowski J. Two-hybrid fluorescence cross-correlation spectroscopy detects protein-protein interactions in vivo. ChemPhysChem 2005;6:984-990.
51. Haralick RMS, K.; Dinstein I. Textural features for image classification. Systems, Man and Cybernetics, IEEE Transactions on 1973;SMC-3:610 - 621.
52. Fischer-Posovszky P, Newell FS, Wabitsch M, Tornqvist HE. Human SGBS cells - a unique tool for studies of human fat cell biology. Obes Facts 2008;1:184-9.
53. Keuper M, Dzyakanchuk A, Amrein KE, Wabitsch M, Fischer-Posovszky P. THP-1 Macrophages and SGBS Adipocytes - A New Human in vitro Model System of Inflamed Adipose Tissue. Front Endocrinol (Lausanne) 2011;2:89.
54. Wabitsch M, Brenner RE, Melzner I, Braun M, Moller P, Heinze E, Debatin KM, Hauner H. Characterization of a human preadipocyte cell strain with high capacity for adipose differentiation. Int J Obes Relat Metab Disord 2001;25:8-15.
55. Otsu N. A threshold selection method from gray-level histograms. IEEE Transactions on Systems, Man and Cybernetics 1979;9:62- 66.
56. Bacso Z, Everson RB, Eliason JF. The DNA of annexin V-binding apoptotic cells is highly fragmented. Cancer Res 2000;60:4623-8.
57. Larsen BD, Rampalli S, Burns LE, Brunette S, Dilworth FJ, Megeney LA. Caspase 3/caspase-activated DNase promote cell differentiation by inducing DNA strand breaks. Proc Natl Acad Sci U S A 2010;107:4230-5.
58. Clegg RM. Fluorescence resonance energy transfer. Curr Opin Biotechnol 1995;6:103-10.
59. Förster T. Fluoreszenz organischer Verbindungen. Göttingen,: Vandenhoeck & Ruprecht; 1951. 312 p. p.
60. Stryer L. Fluorescence energy transfer as a spectroscopic ruler. Annu Rev Biochem 1978;47:819-46.
61. Chalfie M, Tu Y, Euskirchen G, Ward WW, Prasher DC. Green fluorescent protein as a marker for gene expression. Science 1994;263:802-5.
62. Piston DW, Patterson GH, Knobel SM. Quantitative imaging of the green fluorescent protein (GFP). Methods Cell Biol 1999;58:31-48.
63. Bacso Z, Bene L, Bodnar A, Matko J, Damjanovich S. A photobleaching energy transfer analysis of CD8/MHC-I and LFA-1/ICAM-1 interactions in CTL-target cell conjugates. Immunol Lett 1996;54:151-6.
64. Jovin TM, Arndt-Jovin DJ. Luminescence digital imaging microscopy. Annu Rev Biophys Biophys Chem 1989;18:271-308.
65. Szentesi G, Vereb G, Horvath G, Bodnar A, Fabian A, Matko J, Gaspar R, Damjanovich S, Matyus L, Jenei A. Computer program for analyzing donor photobleaching FRET image series. Cytometry A 2005;67:119-28.

66. Szaloki N, Doan-Xuan QM, Szollosi J, Toth K, Vamosi G, Bacso Z. High throughput FRET analysis of protein-protein interactions by slide-based imaging laser scanning cytometry. Cytometry A 2013;83:818-29.
67. Martin ML, Lieberman PM, Curran T. Fos-Jun dimerization promotes interaction of the basic region with TFIIE-34 and TFIIF. Mol Cell Biol 1996;16:2110-8.
68. Hai T, Curran T. Cross-family dimerization of transcription factors Fos/Jun and ATF/CREB alters DNA binding specificity. Proc Natl Acad Sci U S A 1991;88:3720-4.
69. Szollosi J, Tron L, Damjanovich S, Helliwell SH, Arndt-Jovin D, Jovin TM. Fluorescence energy transfer measurements on cell surfaces: a critical comparison of steady-state fluorimetric and flow cytometric methods. Cytometry 1984;5:210-6.
70. Tron L, Szollosi J, Damjanovich S, Helliwell SH, Arndt-Jovin DJ, Jovin TM. Flow cytometric measurement of fluorescence resonance energy transfer on cell surfaces. Quantitative evaluation of the transfer efficiency on a cell-by-cell basis. Biophys J 1984;45:939-46.
71. Sebestyen Z, Nagy P, Horvath G, Vamosi G, Debets R, Gratama JW, Alexander DR, Szollosi J. Long wavelength fluorophores and cell-by-cell correction for autofluorescence significantly improves the accuracy of flow cytometric energy transfer measurements on a dual-laser benchtop flow cytometer. Cytometry 2002;48:124-35.
72. Vamosi G, Baudendistel N, von der Lieth CW, Szaloki N, Mocsar G, Muller G, Brazda P, Waldeck W, Damjanovich S, Langowski J and others. Conformation of the c-Fos/c-Jun complex in vivo: a combined FRET, FCCS, and MD-modeling study. Biophys J 2008;94:2859-68.
73. Doan-Xuan QM, Szaloki N, Toth K, Szollosi J, Bacso Z, Vamosi G. FRET Imaging by Laser Scanning Cytometry on Large Populations of Adherent Cells. Curr Protoc Cytom 2014;70:2 23 1-2 23 29.
74. Novak N, Leung DY. Advances in atopic dermatitis. Curr Opin Immunol 2011;23:778-83.
75. Novak N. An update on the role of human dendritic cells in patients with atopic dermatitis. J Allergy Clin Immunol 2012;129:879-86.
76. Soumelis V, Reche PA, Kanzler H, Yuan W, Edward G, Homey B, Gilliet M, Ho S, Antonenko S, Lauerma A and others. Human epithelial cells trigger dendritic cell mediated allergic inflammation by producing TSLP. Nat Immunol 2002;3:673-80.
77. Nagy G, Doan-Xuan QM, Gaspar K, Mocsai G, Kapitany A, Torocsik D, Bacso Z, Gyimesi E, Remenyik E, Biro T and others. The atopic skin-like microenvironment modulates the T-cell-polarising cytokine production of myeloid dendritic cells, as determined by laser scanning cytometry. Exp Dermatol 2014;23:276-8.
78. Atanassova P. Histochemical and ultrastructural criteria for early differentiation of human subcutaneous adipocytes. Folia Med (Plovdiv) 1998;40:24-7.
79. Granneman JG, Li P, Lu Y, Tilak J. Seeing the trees in the forest: selective electroporation of adipocytes within adipose tissue. Am J Physiol Endocrinol Metab 2004;287:E574-82.
80. Luther EG, William. Laser scatter in clinical applications. In: Adam Wax VB, editor; 2008 03/2008; San Jose, CA. p 686412-686412-13.
81. Verstraeten VL, Renes J, Ramaekers FC, Kamps M, Kuijpers HJ, Verheyen F, Wabitsch M, Steijlen PM, van Steensel MA, Broers JL. Reorganization of the nuclear lamina and cytoskeleton in adipogenesis. Histochem Cell Biol 2011;135:251-61.
82. Tofilon PJ, Meyn RE. Reduction in DNA repair capacity following differentiation of murine proadipocytes. Exp Cell Res 1988;174:502-10.
83. Bill CA, Grochan BM, Vrdoljak E, Mendoza EA, Tofilon PJ. Decreased repair of radiation-induced DNA double-strand breaks with cellular differentiation. Radiat Res 1992;132:254-8.
84. Tofilon PJ, Meyn RE. Influence of cellular differentiation on repair of ultraviolet-induced DNA damage in murine proadipocytes. Radiat Res 1988;116:217-27.
85. Meulle A, Salles B, Daviaud D, Valet P, Muller C. Positive regulation of DNA double strand break repair activity during differentiation of long life span cells: the example of adipogenesis. PLoS One 2008;3:e3345.

86. Nouspikel T. DNA repair in differentiated cells: some new answers to old questions. Neuroscience 2007;145:1213-21.
87. Nouspikel T, Hanawalt PC. DNA repair in terminally differentiated cells. DNA Repair (Amst) 2002;1:59-75.
88. Sjakste N, Sjakste T. Possible involvement of DNA strand breaks in regulation of cell differentiation. Eur J Histochem 2007;51:81-94.
89. Yan S, Li YZ, Zhu XW, Liu CL, Wang P, Liu YL. HuGE systematic review and meta-analysis demonstrate association of CASP-3 and CASP-7 genetic polymorphisms with cancer risk. Genet Mol Res 2013;12:1561-73.
90. Lovric MM, Hawkins CJ. TRAIL treatment provokes mutations in surviving cells. Oncogene 2010;29:5048-60.
91. Taylor DL, Woo ES, Giuliano KA. Real-time molecular and cellular analysis: the new frontier of drug discovery. Curr Opin Biotechnol 2001;12:75-81.
92. Ljosa V, Carpenter AE. Introduction to the quantitative analysis of two-dimensional fluorescence microscopy images for cell-based screening. PLoS Comput Biol 2009;5:e1000603.

8. Acknowledgment

I have never enjoyed a task more than spending time with and learning from the Biophysics and Cell Biology Department members in University of Debrecen.

I am forever indebted to Dr. Zsolt Bacsó for his devoted coaching, limitless tolerance, and patience. I had the unique honor of having trained under his instruction and of many other Professors and Teachers of Biophysics University of Debrecen since 2004. They have taught me much about the science and the art of medicine. I feel that I have stood in the shadow of giants. I sincerely appreciate Prof. Gábor Szabó, Prof. János Szöllősi and Prof. László Fésüs for giving me the opportunities and kind supports to initiate my scientific career.

I am extremely grateful to Szalóki Nikoletta, Kristóf Endre Károly, Anitta Kinga Sarvari, Georgina Nagy, Cimmerer Zsolt and Ixchelt Cuaranta-Monroy for their friendly and productive collaboration.

Despite being far away, my family has always been unwavering in their supports. Many other dear friends have also given me endless encouragements.

The completion of this project would not have been possible without the expertise and devotion of all of you.

Doan Xuan Quang Minh.

This work was performed by support from the Hungarian Scientific Research Fund Grants:
OTKA K77600, K103965, NK 101337, K75752, CK78179, NK105046, OMFB-01626/2006;
the New Hungary Development Plan grants:
TÁMOP-4.2.1/B-09/1/KONV-2010-0007, TÁMOP-4.2.2/B-10/1-2010-0024,
TÁMOP-4.2.2.A-11/1/KONV-2012-0023, TÁMOP-4.2.2.A-11/1/KONV-2012-0025;
and the Baross Gábor Program (REG-EA-09-1-2009-0010).

Register number: DEENKÉTK/367/2014.
Item number:
Subject: Ph.D. List of Publications

Candidate: Quang-Minh Doan-Xuan
Neptun ID: T6X3ZN
Doctoral School: Doctoral School of Molecular Cell and Immune Biology

List of publications related to the dissertation

1. **Doan-Xuan, Q.**, Szalóki, N., Tóth, K., Szöllősi, J., Bacsó, Z., Vámosi, G.: FRET Imaging by Laser Scanning Cytometry on Large Populations of Adherent Cells.
Curr. Protoc. Cytom. Suppl. 70., 1-29, 2014.
DOI: http://dx.doi.org/10.1002/0471142956.cy0223s70

Doan-Xuan, Q. and Szalóki, N. contributed equally to this article.

2. Szalóki, N., **Doan-Xuan, Q.M.**, Szöllősi, J., Tóth, K., Vámosi, G., Bacsó, Z.: High throughput FRET analysis of protein-protein interactions by slide-based imaging laser scanning cytometry.
Cytometry A. 83 (9), 818-829, 2013.
DOI: http://dx.doi.org/10.1002/cyto.a.22315
IF:3.066

Szalóki, N. and Doan-Xuan, Q. M. contributed equally to this article.

3. **Doan-Xuan, Q.M.**, Sárvári, A.K., Fischer-Posovszky, P., Wabitsch, M., Balajthy, Z., Fésüs, L., Bacsó, Z.: High content analysis of differentiation and cell death in human adipocytes.
Cytom. Part A. 83 (10), 933-943, 2013.
DOI: http://dx.doi.org/10.1002/cyto.a.22333
IF:3.066

Doan-Xuan, Q. M. and Sárvári, A. K. contributed equally to this article.

List of other publications

4. Cuaranta-Monroy, I., Simándi, Z., Kolostyák, Z., **Doan-Xuan, Q.**, Póliska, S., Horváth, A., Nagy, G., Bacsó, Z., Nagy, L.: Highly efficient differentiation of embryonic stem cells into adipocytes by ascorbic acid.
Stem Cell Res. 13 (1), 88-97, 2014.
DOI: http://dx.doi.org/10.1016/j.scr.2014.04.015
IF:3.912 (2013)

5. Nagy, G., **Doan-Xuan, Q.**, Gáspár, K., Mócsai, G., Kapitány, A., Törőcsik, D., Bacsó, Z., Gyimesi, E., Remenyik, É., Bíró, T., Szegedi, A.: The atopic skin-like microenvironment modulates the T-cell-polarising cytokine production of myeloid dendritic cells, as determined by laser scanning cytometry.
Exp. Dermatol. 23 (4), 276-278, 2014.
DOI: http://dx.doi.org/10.1111/exd.12342
IF:4.115 (2013)

6. Székvölgyi, L., Imre, L., **Doan Xuan, Q.M.**, Hegedűs, É., Bacsó, Z., Szabó, G.: Flow Cytometric and Laser Scanning Microscopic Approaches in Epigenetics Research.
Methods Mol. Biol. 567, 99-111, 2009.
DOI: http://dx.doi.org/10.1007/978-1-60327-414-2_7

Total IF of journals (all publications): 14,159
Total IF of journals (publications related to the dissertation): 6,132

The Candidate's publication data submitted to the iDEa Tudóstér have been validated by DEENK on the basis of Web of Science, Scopus and Journal Citation Report (Impact Factor) databases.

08 January, 2015

10. Appendix

Other publications related to dissertation:

Abstract:

Doan-Xuan, Q.-M., Szalóki, N., Tóth, K., Szöllősi, J., Bacso, Z. and Vámosi, G. Förster resonance energy transfer analysis of nuclear proteins by laser scanning cytometry.
Eur Biophys J (2011) 40 (Suppl 1):S35–S241, DOI 10.1007/s00249-011-0734-z.

Oral presentation:

1) **Doan-Xuan, Q. M.**, Sarvari, A. K., Fischer-Posovszky, P., Wabitsch, M., Balajthy, Z., Fesus, L. and Bacso, Z. Seeing the cell face, knowing the cell fate. 7th Molecular Cell and Immune Biology Winter Symposium, Galyatető, Hungary, January 7-10, 2014.

2) **Doan-Xuan, Q. M.**, Szalóki, N., Tóth, K., Szöllősi, J., Bacso, Z. and Vámosi, G. Proteins' interaction: don't fret, FRET it. 6th Molecular Cell and Immune Biology Winter Symposium, Galyatető, Hungary, January 8-11, 2013.

3) Nagy, G., **Doan-Xuan, Q. M.**, Gáspár, K., Mócsai, G., Kapitány, A., Törőcsik, D., Bacso, Z., Gyimesi, E., Remenyik, É., Bíró, T. and Szegedi, A. Immunophenotyping by imaging cytometry in atopic dermatitis. 5th Molecular Cell and Immune Biology Winter Symposium, Galyatető, Hungary, 4-7 January, 2012.

4) **Doan-Xuan, Q. M.**, Bacso, Z. Relationship between DNA damage and Annexin V positivity in different apoptosis inductions determined by laser scanning imaging cytometry. Tudományos Diákköri Konferencia, University of Debrecen, April 2-4, 2008.

5) **Doan-Xuan, Q. M.**, Szalóki, N., Tóth, K., Szöllősi, J., Bacso, Z. and Vámosi, G. Fluorescence resonance energy transfer analysis of interaction of cellular proteins using slide based triple-laser cytometry. Tudományos Diákköri Konferencia, University of Debrecen, February 19-23, 2007.

6) **Doan-Xuan, Q. M.**, Bacso, Z. Quantitative detection of DNA fragments by using pulsed-field gel electrophoresis alkaline comet assay and slide-based imaging cytometer. Tudományos Diákköri Konferencia, University of Debrecen, April 10-14, 2006.

Posters:

1) **Doan-Xuan, Q. M.**, Sarvari, A. K., Fischer-Posovszky, P., Wabitsch, M., Balajthy, Z., Fesus, L. and Bacso, Z. High content analysis of differentiation and cell death in human adipocytes. 18th Leipziger Workshop, Cytomics and Congenital Heart Disease, Leipzig, Germany, April 17-19, 2013.

2) Nagy, G., **Doan-Xuan, Q.-M.**, Gáspár, K., Mócsai, G., Kapitány, A., Törőcsik, D., Bacsó, Z., Gyimesi, E., Remenyik, É., Bíró, T. and Szegedi, A. The role of myeloid dendritic cells in the Polarization of effector T cells in atopic dermatitis. 42nd Membrán-Transzport Konferencia, Sümeg, Hungary, May 15-18, 2012.

3) **Doan-Xuan, Q.-M.**, Szalóki, N., Tóth, K., Szöllősi, J., Bacso, Z. and Vámosi, G. Förster resonance energy transfer analysis of nuclear proteins by laser scanning cytometry. 8th European Biophysics Congress (EBSA), Budapest, Hungary, August 23-27, 2011.

Key words:

High content screening, High throughput screening, High content analysis, imaging cytometry, laser scanning cytometry, quantitative cytometry, adipocyte, adipogenesis, DNA damage, DNA break, halo assay, comet assay, FRET, protein interaction, dendritic cell